



Open Archive Toulouse Archive Ouverte (OATAO)

OATAO is an open access repository that collects the work of Toulouse researchers and makes it freely available over the web where possible

This is an author's version published in: <http://oatao.univ-toulouse.fr/19975>

Official URL: <https://doi.org/10.1016/j.ijmultiphaseflow.2018.04.005>

To cite this version:

Butler, Colin  and Lalanne, Benjamin  and Sandmann, Krischan  and Cid, Emmanuel  and Billet, Anne-Marie  Mass transfer in Taylor flow: Transfer rate modelling from measurements at the slug and film scale. (2018) International Journal of Multiphase Flow, 105. 185-201. ISSN 0301-9322

Any correspondence concerning this service should be sent to the repository administrator: tech-oatao@listes-diff.inp-toulouse.fr

Mass transfer in Taylor flow: Transfer rate modelling from measurements at the slug and film scale

C. Butler^{a,b}, B. Lalanne^{a,b}, K. Sandmann^{a,b,c}, E. Cid^{a,b}, A.-M. Billet^{a,b,*}

^aLaboratoire de Génie Chimique, Université de Toulouse, CNRS, Toulouse, France

^bFERMAT, Université de Toulouse, CNRS, INPT, INSA, UPS, Toulouse, France

^cInstitute of Multiphase Flows, Hamburg University of Technology, Hamburg, Germany

ARTICLE INFO

Keywords:

Mass transfer

Taylor flow

PLIF-I

PIV

Lubrication film

ABSTRACT

Mass transfer in non-reactive gas–liquid Taylor flow has been studied at the unit cell scale with high resolution non-invasive experimental techniques for a large variety of hydrodynamic regimes at high inertia ($30 \leq Re_b \leq 1430$). The planar laser induced fluorescence with inhibition (PLIF-I) technique has been used to measure the local oxygen concentration fields in different liquid phases (tap water, water and Breox solutions at different concentrations) in order to vary the Schmidt number Sc . The concentration field can be separated into a film region, corresponding to the thin lubrication film extended all along the channel wall, and the remainder of the liquid which makes up the slug region. It has been found that even though the global mass transfer is mainly driven by the rate of transfer in the slug, the film plays a significant role as a source of oxygen, in addition to the bubble caps, to feed the slug.

In the investigated circular capillary, fed by means of a T-mixer, two contrasted configurations have been observed in the liquid phase (slugs and films), depending on a critical bubble Reynolds number of ~ 300 , where the time-averaged concentration fields are found to differ considerably. For large Reynolds number, particle image velocimetry (PIV) measurements have revealed low temporal fluctuations at the rear of the bubble, possibly due to the presence of adsorbed contaminants, that tends to increase mixing in the slug. Despite this difference, the mass transfer dynamics were found to be controlled in all cases by the intensity of the recirculating motion in the slug, which is directly related to the bubble velocity for these cases of thin films.

A new scaling law has been proposed for the overall Sherwood number, based on Re_b and Sc , which satisfactorily describes the overall mass transfer of the experimental results for $Re_b > 120$ to an accuracy of $\pm 11\%$.

1. Introduction

Many physical systems of various applications utilise two-phase segmented flows, such as evaporating or condensing devices. Over the past number of decades, cutting edge technologies of gas–liquid reactors have appeared, such as micro-reactors and monolithic reactors, where intermittent series of bubbles and slugs (so-called Taylor flow) are present. These systems offer a high surface-to-volume ratio, efficient wall heat exchange, inclusion of satisfying catalytic surface, together with moderate pressure drop and better controllability of the reacting system (Machado et al., 2005). When operated in the Taylor flow regime, these systems also allow enhanced mass transfer between phases (Kreutzer et al., 2005;

Shao et al., 2010). Although the size of ducts or channels (either of rectangular or circular cross-section) used in these systems range from the micrometre to centimetre scale, the considered flows all show confined bubbles (their shapes depending on bubble velocity and fluid properties) surrounded by a thin lubrication film (Taylor, 1961; Aussillous and Quéré, 2000; Fletcher and Haynes, 2017). The flow is generally driven by inertial effects (Kreutzer et al., 2005), the Weber number being greater than the capillary number.

For most of the target applications, mass transfer between gas and liquid is a key issue. In particular, it often controls reaction yield in chemical reactors. However, mass transfer rate has been shown to strongly depend on capillary diameter and on bubble shape, length and velocity (Haghnegahdar et al., 2016; Hayashi et al., 2014). In the same way, two contributions to gas–liquid mass transfer occur simultaneously within Taylor flow: transfer from the

* Corresponding author at: Laboratoire de Génie Chimique, Université de Toulouse, CNRS, Toulouse, France.

E-mail address: annemarie.billet@ensiacet.fr (A.-M. Billet).

Nomenclature

A	area (m ²)
C	volumetric average concentration in one unit cell (mg/L)
C^*	maximum theoretical concentration (mg/L)
Ca	capillary number (dimensionless), $\mu_l u_b / \sigma$
D	mass diffusivity (m ² /s)
d	capillary diameter (m)
Eo	Eötvös number (dimensionless), $(\rho_l - \rho_g)gd^2 / \sigma$
g	gravitational acceleration (m/s ²)
h	pixel height (m)
k_L	liquid side mass transfer coefficient (m/s)
K_{SV}	Stern–Volmer constant (L/mg)
N	number of pixels (dimensionless)
n	distance normal to bubble interface (m)
m_{O_2}	mass of dissolved oxygen (mg)
L	length (m)
$[O_2]$	oxygen concentration (mg/L)
Pe_b	bubble Peclet number (dimensionless), $u_b d / D$
Re_b	bubble Reynolds number (dimensionless), $\rho_l u_b d / \mu_l$
r	radius (m)
r_0	radial position of recirculation centre (m)
r_1	radial position of dividing streamline (m)
Sc	Schmidt number (dimensionless), $\mu_l / (\rho_l D)$
Sh	Sherwood number (dimensionless), $k_L d / D$
t	time (s), z / u_b
u	velocity (m/s)
u_{gs}	superficial velocity of gas phase (m/s)
u_{ls}	superficial velocity of liquid phase (m/s)
u_{tp}	two-phase velocity (m/s), $u_{gs} + u_{ls}$
Vol	volume (m ³)
W	relative bubble rise velocity (dimensionless), $(u_b - u_{tp}) / u_b$
We	Weber number (dimensionless), $\rho_l u_b^2 d / \sigma$
x, y	cylindrical coordinates (m or px)
z	distance from channel inlet (m)

Acronyms

PIV	Particle Image Velocimetry
PLIF-I	Planar Laser Induced Fluorescence with Inhibition

Greek

δ	lubrication film thickness (m)
ε_g	gas hold-up (dimensionless)
μ	dynamic viscosity (Pa s)
ρ	density (kg/m ³)
σ	surface tension (N/m)
τ	shear stress (Pa)
φ	rate of mass transfer (kg/s)

Subscripts

1,2	experimental measurement positions along channel
b	bubble
cir	circulation in slug
cor	corrected
$film$	lubrication film
g	gas phase
l	liquid phase
s	slug
tp	two-phase
uc	unit cell

bubble caps to liquid slug, and transfer from bubble to the lubrication film (Haase et al., 2016). Each of these two contributions can be predominant or negligible, depending on the situation (physical absorption of gas with possible saturation of the films, or reacting walls with dissolved gas concentration (Van Baten and Krishna, 2004). Many predictive empirical relations have been derived in literature, scaling the Sherwood to the Peclet or Eötvös numbers (Haase et al., 2016; Hosoda et al., 2014; Kastens et al., 2015), or relating the volumetric (liquid side) mass transfer coefficient $k_L a$ to operational parameters like phase superficial velocities, bubble and slug lengths (Van Baten and Krishna, 2004; Sobieszuk et al., 2012). However, these scaling laws have been found to be valid in the conditions of establishment only. Each specific case or system therefore needs to be investigated individually. Furthermore, due to the lack of local data, the insights into the complex coupled contributions to mass transfer (Abiev, 2013) are still rarely found in literature. For a good understanding and prediction of phase interactions and mass transfer, the local phenomena need to be investigated by use of non-invasive and high spatial resolution techniques.

The planar laser-induced fluorescence technique with inhibition (PLIF-I) has been used for a decade and can be applied to various gas–liquid systems, like free rising bubbles (Dani et al., 2007; Valiorgue et al., 2013; Häber et al., 2015; Jimenez et al., 2013a) or confined interfaces (Jimenez et al., 2013b; Roudet et al., 2017; Kastens et al., 2017). This technique is based on the use of specific dyes whose fluorescence can be quenched by the presence of dissolved gas.

When rigorously applied, this technique allows for the recording of images of the dissolved gas concentration field. Instantaneous and time-averaged dissolved gas concentration fields, measured by PLIF-I technique, exhibit well contrasted patterns even close to the gas–bubble interface (Butler et al., 2016). However, the signal to noise ratio may be poor if the laser does not excite the dye at an optimised wavelength. Furthermore, incident and fluorescence light may be reflected on the wall and bubble interface, leading to data processing difficulties and non-negligible uncertainties. To account for these issues, laser wavelength should be adjusted to the maximum dye absorption, and a specific data processing methodology should be implemented to take light scattering into account.

Additionally, the well-known particle image velocimetry (PIV) technique allows for the possibility to measure the local velocity flow fields. This technique is based on tracking the motion of seeded particle groups by pulsed laser illumination and imaging of the light scattering within a small time interval (Charogiannis et al., 2015). It has been previously employed in the study of μ -scale Taylor flow (King et al., 2007; Meyer et al., 2014), single Taylor bubbles rising in a column (Bugg and Saad, 2002; Van Hout et al., 2002; Nogueira et al., 2006) and Taylor bubble train flows (Thulasidas et al., 1997; Tsoligkas et al., 2007). These studies confirm the presence of counter-rotating vortices present in the liquid phase, which was first reported by Taylor (1961). These vortices drive the mixing process in the slugs (Thulasidas et al., 1997). Most of the studies only describe the time-averaged flow field in the slugs; however, an analysis dedicated to the instantaneous flow fields becomes necessary at large Reynolds numbers in order to quantify any fluctuations.

The aim of this study is to investigate the mass transfer dynamics in non-reactive gas–liquid Taylor bubble train flow in a circular capillary, based on the experimental concentration fields obtained in high resolution by the PLIF-I technique, for a large variety of hydrodynamic regimes. The main advantage of this method is the acquisition of accurate information about mass transfer in both slugs and films, allowing for the separation of their roles to the overall gas absorption rate. The study is restricted to regimes where the

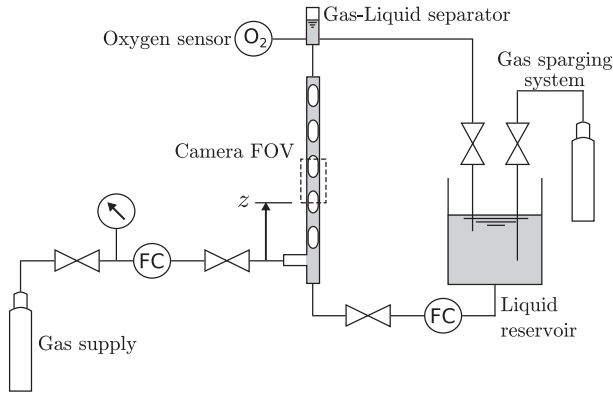


Fig. 1. Schematic of the experimental test-rig.

Taylor flow is stable (i.e. without noticeable oscillation in bubble and/or slug length) and where both the bubble shape and concentration fields are axisymmetric. The occurring phenomena are further interpreted thanks to PIV measurements. Based on this data of contrasting regimes over a large range of parameters, a correlation for the mass transfer rate as a function of some of the non-dimensional numbers relevant for this problem is proposed.

2. Materials and methods

2.1. Experimental test-rig

For the detailed investigation of Taylor bubbles an experimental set-up has been designed that enables well-defined and reproducible Taylor bubble flows. It consists of a single channel in which the gas-liquid interaction is observed (see Fig. 1). The channel is a vertical glass tube with a circular cross-section, an internal diameter d of 3 mm (± 0.01 mm) and a height of 1.2 m. The gas is injected into the liquid through a T-junction located at the channel inlet. It can be set up so that either ascending or descending concurrent flow can be generated. The gas flow rate is regulated by a Brooks SLA580S mass flow meter connected to a West 6100+ digital controller. The liquid phase is supplied from a 20 L reservoir tank and is circulated in a closed loop by a Tuthill D-series gear pump with the flow rate regulated by a Bronkhorst mini CORIFLOW mass flow controller. The gas bubbles and liquid slugs flow through the channel and are separated at the outlet. The gas is exhausted to the ambient atmosphere and the liquid returns to the reservoir tank. A gas sparging system is included in the liquid reservoir tank which allows the liquid to be completely deoxygenated before it enters the channel by continuously bubbling nitrogen gas.

A Unisense OX-50 micro-sensor probe connected to a Unisense PA2000 amplifier was placed at the channel outlet. This sensor was used to measure the total mass transfer along the channel length.

In these experiments, oxygen was used as the fluid for the gas phase. For reference and calibration purposes, nitrogen gas was also used. For the liquid phase, tap water or a water-Breox 75 W 55,000 solution was used. Breox 75 W 55,000 is a product sold by BASF SE, called “polyalcoxyther” or “Tergitol” (CAS number 9003-11-6). It is a block co-polymer of ethylene glycol and propylene glycol, which offers a high viscosity (up to 60 Pa s at 40 °C) and is completely soluble in water. It was used to vary the viscosity of the liquid phase and hence the Schmidt and Capillary numbers. 5% and 10% m/m Breox in water solutions were prepared. The liquid physical properties of the different liquid solutions (containing the fluorescent dye used for the PLIF-I measurements) were measured in-house and are presented in Table 1. The mass diffusivities

Table 1
Liquid physical properties at 25 °C.

Liquid	ρ (kg/m ³)	$\mu \pm 4\%$ (Pa s)	σ (N/m)	D (m ² /s)
Water	998	1.05×10^{-3}	71.2×10^{-3}	2.00×10^{-9}
5% m/m Breox-water	1006	4.20×10^{-3}	52.2×10^{-3}	1.70×10^{-9}
10% m/m Breox-water	1012	9.20×10^{-3}	52.0×10^{-3}	1.31×10^{-9}

of water-Breox solutions were measured following the protocol described in Xu et al. (2017).

Rheology of the two water-Breox solutions were measured under different applied shear stresses τ . For $0.1 \text{ Pa} \leq \tau \leq 20 \text{ Pa}$, viscosity can be considered as constant, hence these solutions behave as Newtonian fluids, whereas, for lower τ , shear thinning is observed. In our experiments with Breox solutions (see full list of regimes in Table 2), the maximum value of τ at the channel wall lies between 0.9 Pa (regime 11) and 6.8 Pa (regime 14). Thus, the linearity of the radial profile of τ in a tube shows that the hypothesis of a Newtonian fluid is valid, provided $x \geq d/18$ in the worst condition (regime 11); we will therefore assume a uniform viscosity for these Breox solutions in the whole capillary for regimes 11–14.

2.2. Imaging systems and setup

In order to keep the complexity of the experimental set up and testing to a minimum, the PLIF-I, PIV and shadowgraphy measurements were not performed simultaneously. The PLIF-I and shadowgraphy experiments were conducted during the same test campaign for the mass transfer measurements. The experimental set up allows for the capture of the PLIF-I and shadowgraphy images one after the other without any movement of equipment or disturbance of the flow in the channel. It was simply necessary for the required light source to be activated and the camera set to the corresponding frequency of acquisition. The PIV experiments were conducted during a second test campaign for the velocity measurements.

A glycerol filled visualisation box was placed around the glass tube during the experiments. As the refractive indices of glycerol and glass are almost identical, any refraction or reflection of light as it passes through the channel walls becomes negligible (Häber et al., 2015; Thulasidas et al., 1997).

2.2.1. Shadowgraphy setup

The shadowgraphy technique is a well-known visualisation technique which involves illuminating the subject of study by a diffuse light source and recording images of its shadow (Settles, 2001). The camera used for the shadowgraphy imaging was a PCO Edge 5.5 sCMOS camera. Its resolution was reduced to 2560×402 pixels to image the channel area of interest only and allow for a higher frequency of acquisition of 100 Hz. An exposure time of 100 μ s was used to effectively freeze the flow. The camera was fitted with a Nikon 105 mm macro f/2.8 lens and a series of extension tubes with a total length of 68 mm. A 120×160 mm Phlox LED panel was used as a continuous light source. It was positioned directly behind the channel, perpendicular to the axis of the camera.

2.2.2. PLIF-I setup

The basic principle of the PLIF-I technique takes advantage of the fluorescent quenching behaviour of molecular oxygen to certain fluorophores. This quenching is governed by the Stern-Volmer equation

$$\frac{I_{0,x,y}}{I_{x,y}} = 1 + K_{SV,x,y}[O_2]_{x,y} \quad (1)$$

where I_0 and I are the fluorescent intensities in the absence and the presence (respectively) of the dissolved oxygen, $[O_2]$ is the concentration of dissolved oxygen, K_{SV} is the Stern–Volmer constant, and x and y correspond to the spatial coordinates of a given pixel on the camera sensor. The fluorescent tracer used in these experiments is Dichlorotris (1,10-phenanthroline) ruthenium(II) hydrate ($[Ru(phen)_3]$) (CAS No. 207802-45-7). This tracer has been used previously in the literature for oxygenation measurements (O’Neal et al., 2004; Huntsova et al., 2014; Jimenez et al., 2014; Janke and Bauer, 2017). The tracer is directly soluble in the liquid phase and is used at a low concentration of 50 mg/L. As a consequence, it does not significantly alter the liquid properties, and presents constant calibration properties (Jimenez et al., 2014).

The light source used to excite this tracer was an Oplette Opolette 355 tunable laser system. The advantage of using this system is that it can generate wavelengths over a broad range and therefore allows for the tuning of the laser light to the maximum excitation frequency of the tracer being used. By exciting the tracer at its maximum absorption wavelength of 450 nm, the resulting emission is maximised and images with excellent dynamic range are produced. The emission intensities are related to the dissolved O_2 concentration by Eq. (1). By comparing images produced with a Nd:YAG laser (wavelength of 532 nm), it was found that those produced with the Opolette laser (5 mJ) had a dynamic range three times greater. A motorised attenuator assures the stability of the laser energy pulses, with a measured standard deviation of less than 5% between pulses.

The laser system was equipped with a lens system which produces a diverging laser sheet with a measured thickness of 280 μm . The light sheet was positioned to pass through the centreline of the channel and perpendicular to the axis of the camera.

As mentioned at the start of this section, the shadowgraphy and PLIF-I imaging was conducted during the same campaign, therefore the same camera setup was used. The camera was set to an acquisition frequency of 20 Hz with an exposure time of 100 μs . The frequency of acquisition is limited by the maximum repetition rate of the laser system. The excited lifetime of the Ruthenium tracer complex is $< 20 \mu\text{s}$ (Nakamaru, 1982) meaning there can be no cumulative effect of the fluorescent signal due to multiple excitations from the laser. A 540 nm OD 6 high pass filter was placed in front of the camera to block the light at the laser wavelength but allow the resulting light at the fluorescent wavelengths to pass.

2.2.3. PIV setup

Time-resolved particle image velocimetry measurements were carried out in the same plane as the PLIF-I images, passing through the centreline of the channel. A Pegasus laser from New Wave delivering $2 \times 8 \text{ mJ}$ at 532 nm, operating at 500 Hz, and a CMOS camera RS3000 (Photron) with a resolution of 1024×220 pixels were used. The camera was equipped with the same 105 mm Nikon lens, extension tubes and high pass filter that were used for the PLIF-I measurements. Fluorescent polystyrene particles (PS Fluo-Red) with a mean diameter of 10 μm were used as seeding particles in the liquid phase. The system allowed the acquisition of pairs of images at a rate of 500 Hz. These pairs were analysed using Davis 8.4 software (Lavis) using 75% overlapping windows of 32×32 pixels, yielding fields of 128×21 vectors with a spatial resolution of 0.135 mm ($0.045d$) in the axial direction.

2.3. Experimental procedure for mass transfer measurements

The mass transfer measurements are obtained from the shadowgraphy and PLIF-I imaging, as well as from the O_2 micro-sensor probe. Pure O_2 was used as the gas phase. Given gas and liquid flow rates were set on the corresponding controllers, and 5000 shadowgraphy and PLIF-I images were recorded once the flow was

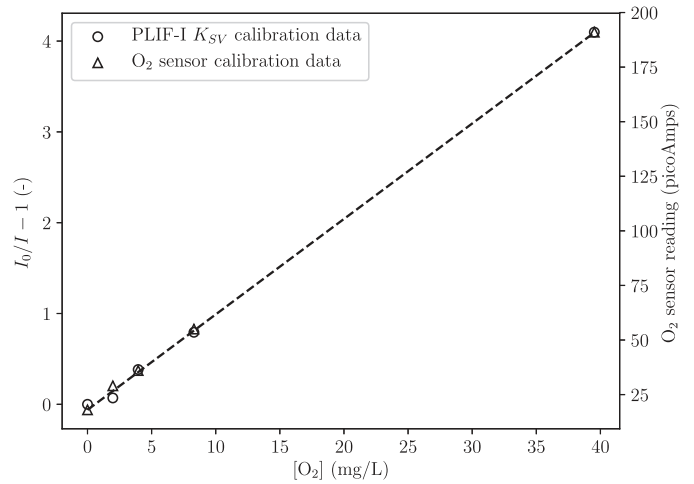


Fig. 2. An example of a calibration curve for determination of the Stern–Volmer constant for a pixel from the interrogation window; also shown the calibration curve of the O_2 sensor probe (water as liquid phase).

stabilised. Examples of recorded instantaneous shadowgraphy and PLIF-I images are shown in Figs. 3 and 4. This procedure was repeated for all of the Taylor flow regimes observed in this study. The position z of the camera and the laser was then moved to a second position a certain distance further away from the channel inlet and the measurements were repeated for the same range of flow rates. This means that four O_2 concentration values can be quantified along the channel length for a given flow regime: at the inlet ($z = 0$), at two positions (z_1, z_2) along the channel (values of z_1 and z_2 depend on the considered regime), and at the outlet ($z = 1.2 \text{ m}$).

A number of important calibration steps are required for the mass transfer measurements. The first includes the determination of K_{SV} in Eq. (1) at each of the two positions along the channel for the PLIF-I images. The calibration procedure involves saturating the liquid at known O_2 concentration values and recording the resulting fluorescence by the camera (Dani et al., 2007). This was achieved by bubbling mixtures of O_2 and N_2 gas inside the liquid reservoir at 0% (pure N_2), 5%, 10%, 21% (air) and 100% (pure O_2) for long durations (more than 30 min) to ensure saturation of the liquid phase. Saturation (and thus steady state) was confirmed by the stabilisation of the O_2 sensor signal. For a given concentration, 100 images were used to create an average image and the value of K_{SV} could then be determined by a linear regression fit of the data, pixel by pixel, as shown in Fig. 2, where the slope of the line is equal to K_{SV} for a given pixel. This type of calibration procedure therefore accounts for laser light sheet non-uniformity, absorption, pixel response non-uniformity and lens vignette (Valiorgue et al., 2013; Webster et al., 2001). At the same time as these calibrations, the O_2 sensor probe was also calibrated. The electrical signal from the probe was related to the known O_2 concentrations using a linear regression fit, as shown in Fig. 2.

A spatial calibration step was necessary to determine the magnification factor to convert from pixels to physical units of measure. To do this, a checkerboard pattern, consisting of a grid of 15×15 squares, each 193 μm ($\pm 0.68 \mu\text{m}$) in width, was suspended inside the channel in the camera’s field of view. Due to refraction effects between the glass channel and internal liquid, pixel width in the radial direction increases with distance from the channel axial centreline. These effects have been taken into account using the Snell–Descartes law, which involves a series of trigonometric operations coupled with the geometrical optics of light refraction (Mac Giolla Eain et al., 2013). A constant magnification factor was applied in the axial direction.

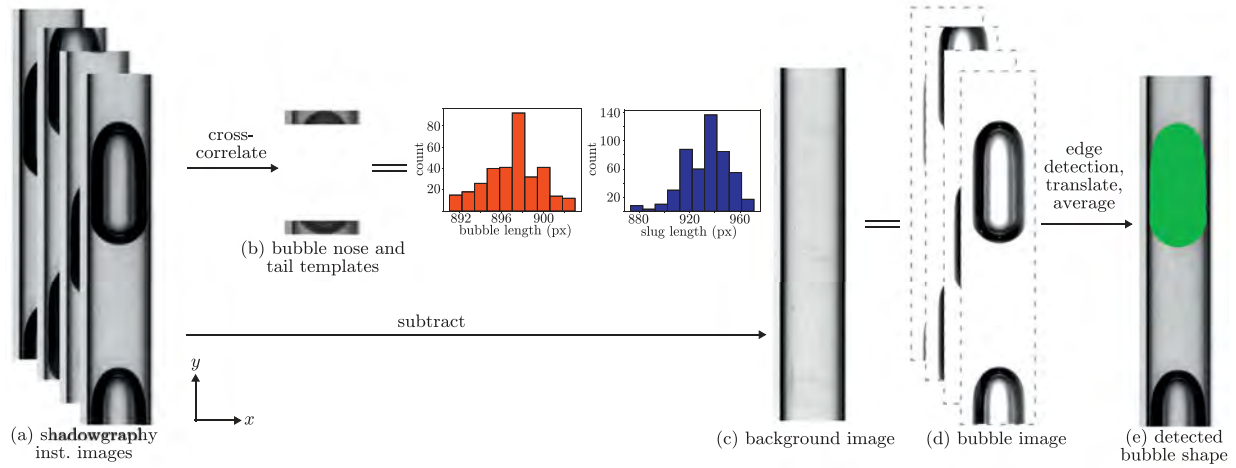


Fig. 3. Shadowgraphy image processing using data for regime 9.

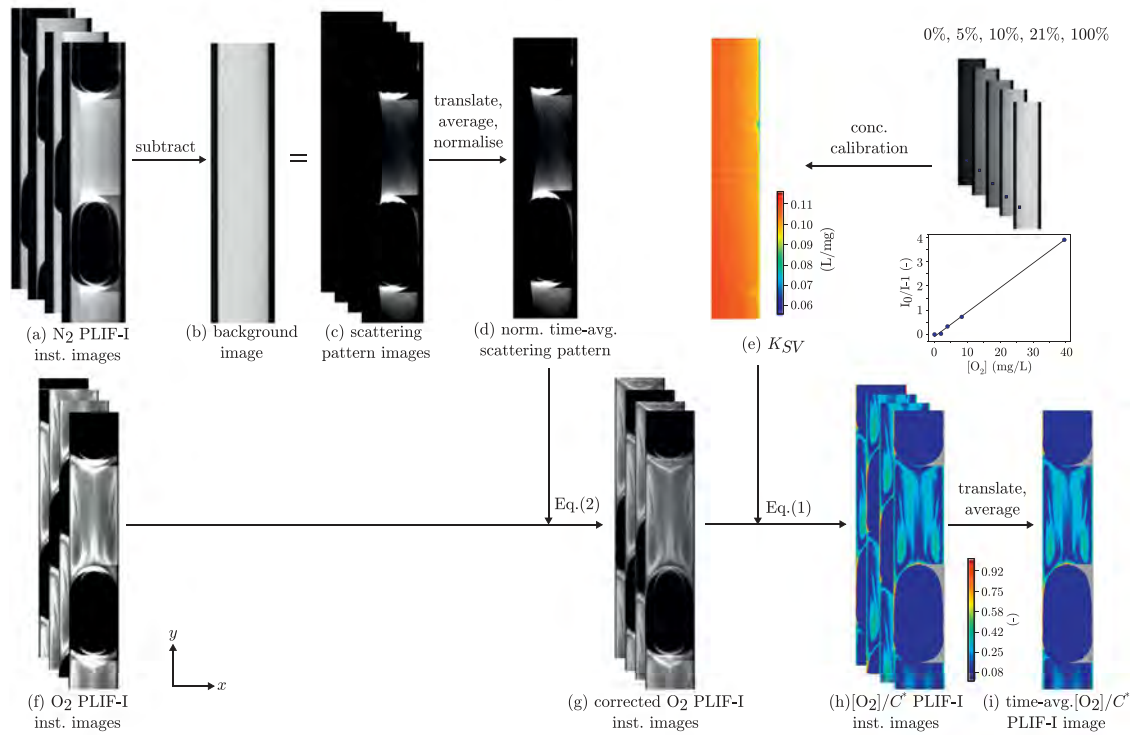


Fig. 4. PLIF-I image processing using data for regime 9.

In order to account for light scattering effects due to the reflection and refraction of the laser light as it passes through the bubble interface, the mass transfer measurements were repeated by replacing O_2 with N_2 as the gas phase. This scattering effect can be seen in Fig. 4(a) as the areas of increased intensity close to the bubble interface. It is assumed that no mass transfer takes place between the N_2 gas bubbles and the de-oxygenated liquid phase, and therefore, there should be no spatial variations due to quenching of the fluorescence signal as the dissolved O_2 concentration is uniform and equal to 0. As a consequence, the N_2 images can serve as a reference, whereby the level of increased intensity can be quantified and then removed from the O_2 images. The procedure to apply this correction is detailed in Section 3.1.2 and validated in Section 3.1.3.

3. Image processing

3.1. Mass transfer measurements

In order to extract the data related to the mass transfer phenomena occurring between the two fluids, significant processing of the shadowgraphy and PLIF-I images was required. All the image processing was performed using MATLAB, and computationally intensive tasks were performed using a GPU by integrating custom CUDA kernels.

3.1.1. Shadowgraphy images

The shadowgraphy images were used to determine the physical characteristics and some hydrodynamic data of a given flow regime.

The first step in the processing of all the images is the determination of the phases. The locations of the solid channel walls (seen as the dark vertical bands on the left and right of the images in Fig. 3(a)) were found from an edge detection algorithm, where an edge location was associated with a local peak in the gradient image intensity values in the radial direction.

To find the position(s) of the bubble(s) in each image, each image was cross-correlated with template images of the bubble nose and tail (see Fig. 3(b)). An algorithm was then used to sort the calculated bubble nose and tail axial positions in each image and to understand the order of the phases, i.e. from the bottom to the top of an image: partial gas bubble – liquid slug – gas bubble – partial liquid slug, or partial liquid slug – gas bubble – partial liquid slug, etc. This information was important as it was then used to calculate the bubble and slug lengths, L_b and L_s , respectively, with the aid of the spatial calibration. The average length L_{uc} of the unit cell can then be deduced for each studied regime, as defined by $L_{uc} = L_b + L_s$.

To isolate the complete gas–liquid bubble interface, a background image was firstly subtracted from the instantaneous image. The background image consists of an image with no gas phase present (see Fig 3(c)). The result of the subtraction was an image which only contains the gas bubble(s) (see Fig. 3(d)). Using a technique similar to that for the channel wall positions, the interface could then be traced. Assuming axial symmetry, an integration of the interface profile about the centreline gives the bubble volume. Thus the value of gas hold up, $\varepsilon_g = Vol_b/Vol_{uc}$, was calculated, where $Vol_{uc} = \pi d^2 L_{uc}/4$.

The time-averaged bubble velocity u_b was calculated from the displacement of a bubble from one image to the next and the camera frequency of acquisition. The displacement is obtained by cross-correlating two successive image frames. This method gives a precision of 1×10^{-3} m/s in the calculation of u_b .

3.1.2. PLIF-I images

The PLIF-I images were used to determine the concentration of dissolved oxygen $[O_2]$ in the liquid phase. The image processing is summarised in Fig. 4.

As mentioned earlier in Section 2.3, two sets of PLIF-I images were required for a given Taylor flow regime – one using O_2 as the gas phase, and a second using N_2 . The N_2 images served as references in order to quantify the scattered light so it could then be corrected for in the O_2 images.

The pattern and intensities of scattered light were found by subtracting the N_2 images with a background image. The background image is defined as an image with no gas phase present, and in which the liquid is completely saturated with N_2 . For each pixel of the image, this corresponds to $I_{0,x,y}$ in Eq. (1). The scattering pattern image (see Fig. 4(c)) shows the zones of increased intensity close to the bubble interface as the areas of increased intensity in the liquid phase. The scattering pattern image was normalised by dividing it by the instantaneous N_2 image to find the relative increase in intensity, pixel-by-pixel. A time-averaged scattering pattern image (see Fig. 4(d)) was then created by translating the images in the axial direction so the bubbles and slugs are aligned. This translation distance was determined for each image by cross-correlating an image with templates of the bubble nose and tail, similar to the process used for the shadowgraphy images. Of the 5000 images recorded, only those which had a slug length exactly equal to the median slug length, determined from the cross-correlation step, were used to create the time-averaged images. This was done to ensure the slugs and quenching patterns aligned correctly when they were translated before time-averaging. On average, approximately 400 of the 5000 images were used in the final time-averaged images.

Then, in order to correct the instantaneous O_2 images, the following equation was applied pixel-by-pixel, assuming that, at each considered pixel, the scattering effects have the same relative order of magnitude for any average value of $[O_2]$,

$$I_{cor,x,y} = I_{x,y} \left[1 - \left(\frac{\bar{I}_{N_2,x,y} - \bar{I}_{0,x,y}}{\bar{I}_{N_2,x,y}} \right) \right] \quad (2)$$

where I_{cor} is the corrected pixel intensity, $I_{x,y}$ is the uncorrected instantaneous intensity, and the terms in the round parenthesis correspond to the normalised scattering pattern image produced from the subtraction process of the N_2 images and the background image. After applying Eq. (2), the discontinuities present in quenching patterns are no longer visible (see Fig. 4(g)).

Before creating the time-averaged $[O_2]$ image, the instantaneous images were first converted from grayscale intensity values to $[O_2]$. For this, Eq. (1) is used as the K_{SV} calibration is designed to work pixel-by-pixel. Fig. 4(h) shows the images converted into $[O_2]/C^*$. This maximum value C^* is the theoretical saturation of $[O_2]$ in water calculated from Henry's law (Sander, 2015), and used for calibration. In the case where liquid phase is a mixture of water and Breox (regimes 11–14), C^* is unknown. It can be assumed to be close to the C^* value for water, as the mixtures contain 10% of Breox at maximum. However, it is preferred here to express all concentration data through the calibrated normalised values $[O_2]/C^*$ in these cases. The time-averaged image was created from translating the instantaneous images along the axial centreline.

The area of interest in the time-averaged $[O_2]$ image is the unit cell, i.e. one complete bubble and slug. The data hidden by the bubble shadow during the PLIF-I measurements, seen as the area of reduced intensity to the right of the bubbles in Fig. 4, as well as the bubble itself, cannot be exploited. However, as the unit cell is expected to be axisymmetric, the total mass of dissolved O_2 in the liquid phase can be calculated by the summation of the concentration of each pixel multiplied by the cylindrical shell volume of each pixel,

$$m_{O_2} = \sum_{y=1}^{N_y} \sum_{x=1}^{N_x} [O_2]_{x,y} [\pi (r_{x,y}^2 - r_{x-1,y}^2) h] \quad (3)$$

where r is the radius of a cylindrical shell, h is the height of a pixel and N is the number of pixels. As stated above, due to the axisymmetry, the pixels were integrated only on the left hand side of each image with respect to the axis of symmetry. Note that from knowing the positions of the bubble nose and tail from the cross-correlation step, and the shape of the bubble interface, determined from the shadowgraphy images in Section 3.1.1, the values of $[O_2]$ inside the bubble were first set to 0 before applying Eq. (3) so as not to be included in the calculation of m_{O_2} .

3.1.3. Scattered light image correction validation tests

In order to assess the correction methodology used during the PLIF-I image processing, described in the previous section, a Taylor flow regime was generated with known gas and liquid concentrations. This was achieved by pre-saturating water in the reservoir with air and using air as the gas phase. When the two phases enter the channel, as they are equilibrated values of $[O_2]$, no O_2 mass transfer takes place, however the light scattering phenomenon was still present and results in an increased intensity signal as seen by the camera.

The time-averaged mass of dissolved O_2 was calculated for this regime, both with and without the application of Eq. (2). It was then compared to the theoretical value of the m_{O_2} in the identical liquid slug completely saturated with air. For this case with no correction, the total value of m_{O_2} was underestimated by 22%, whereas the case with the correction results in an underestimation

Table 2
Summary of experimentally measured Taylor flow regimes.

Regime No	Liquid phase	Config.	u_{gs} (m/s)	u_b (m/s)	u_{tp} (m/s)	u_b (m/s)	Re_b	Sc	Ca	We
1	Water	Asc.	0.022	0.020	0.041	0.042	1.2×10^2	5.3×10^2	6.1×10^{-4}	0.1
2	Water	Asc.	0.047	0.039	0.086	0.092	2.6×10^2	5.3×10^2	1.4×10^{-3}	0.4
3	Water	Asc.	0.045	0.079	0.124	0.140	4.0×10^2	5.3×10^2	2.1×10^{-3}	0.8
4	Water	Asc.	0.088	0.098	0.186	0.210	5.9×10^2	5.3×10^2	3.1×10^{-3}	1.9
5	Water	Asc.	0.084	0.149	0.233	0.274	7.8×10^2	5.3×10^2	4.0×10^{-3}	3.2
6	Water	Asc.	0.177	0.118	0.295	0.338	9.6×10^2	5.3×10^2	4.9×10^{-3}	4.8
7	Water	Asc.	0.222	0.118	0.340	0.393	1.1×10^3	5.3×10^2	5.8×10^{-3}	6.5
8	Water	Asc.	0.274	0.141	0.415	0.501	1.4×10^3	5.3×10^2	7.4×10^{-3}	10.6
9	Water	Asc.	0.103	0.143	0.246	0.283	8.1×10^2	5.3×10^2	4.2×10^{-3}	3.4
10	Water	Des.	0.056	0.161	0.217	0.240	6.8×10^2	5.3×10^2	3.5×10^{-3}	2.4
11	5% m/m Breox-water	Asc.	0.042	0.039	0.081	0.097	7.0×10^1	2.5×10^3	7.8×10^{-3}	0.5
12	5% m/m Breox-water	Asc.	0.157	0.118	0.285	0.373	2.7×10^2	2.5×10^3	3.0×10^{-3}	8.0
13	10% m/m Breox-water	Asc.	0.039	0.078	0.078	0.097	3.2×10^1	6.9×10^3	1.7×10^{-2}	0.5
14	10% m/m Breox-water	Asc.	0.158	0.118	0.276	0.381	1.3×10^2	6.9×10^3	6.7×10^{-2}	8.5

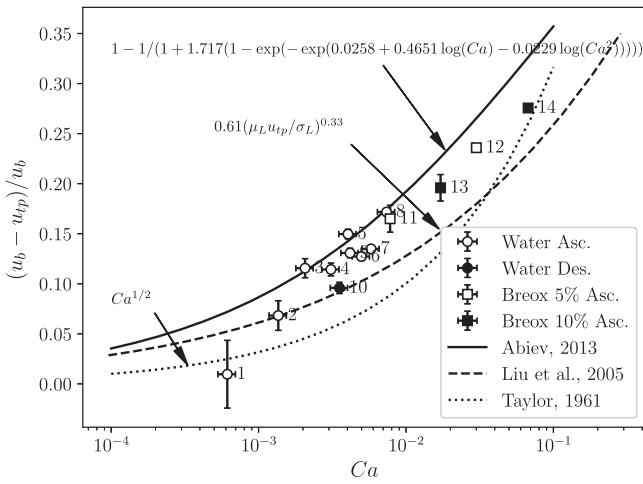


Fig. 5. Relative bubble rise velocity experimental measurements compared to correlations from literature.

of 5% when compared to the theoretical value. The former underestimation is due to the increased signal intensity and the reduction in observed fluorescence quenching. The latter can be adopted as the experimental $[O_2]$ uncertainty values for the PLIF-I measurements in this work.

3.2. PIV images

As mentioned in Section 2.2.3, double-frame PIV images were acquired at a frame rate of 500 Hz. The time delay between each frame was chosen depending on the maximum particle displacement for each flow regime, and ranged from 140 to 1600 μs . In order to provide average quantities, each of the double-frame PIV images was, first, translated to the same reference position in the field of view. This was achieved by template matching of nose bubble in PIV images, as for the PLIF-I images. In a second step, each velocity field was calculated and then time-averaged. Mean velocity and root-mean-square velocity fields can be calculated for each flow regime from a thousand double frame PIV images. Statistical convergence has been checked for mean and fluctuating velocities.

As for mass transfer measurements, the same spatial calibration procedure was applied to PIV velocity fields.

4. Results and discussions

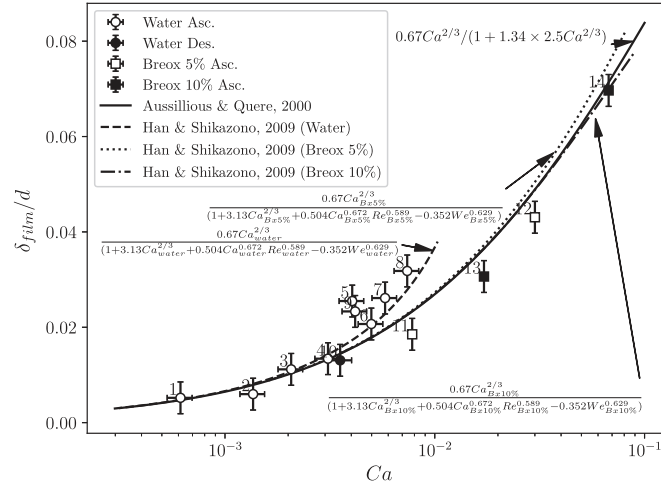
In this work, 14 different hydrodynamic regimes were considered, either ascending or descending con-current flows, as shown below in Table 2. The geometry of Taylor flows obtained were formed of bubble trains composed of unit cells of length $2.9 \leq \frac{L_{uc}}{d} \leq 5.7$, including both short and long slugs, whose lengths were in the range $0.7 \leq \frac{L_s}{d} \leq 3.1$. The hydrodynamics are characterised by a range of moderate to high Reynolds numbers (based on channel diameter and bubble velocity) $30 \leq Re_b \leq 1430$ and a range of low capillary numbers $6 \times 10^{-4} \leq Ca \leq 6 \times 10^{-2}$. These values are associated to Weber numbers $0.1 \leq We \leq 10.6$. Thus, inertial forces are always dominant compared to the viscous forces in these experiments. In some cases however, capillarity is dominant over inertia (low We) such as for regimes 1–2–3–11–13, whereas inertia dominates capillarity for all other regimes (large We). Note also that the Eötvös number is always of order 1 ($1.2 \leq Eo \leq 1.7$). Concerning mass transfer, through the use of different liquids (tap water, solutions of Breox 5% and Breox 10%), the Schmidt number is varied over the range $520 \leq Sc \leq 6940$.

4.1. Relative bubble rise velocity

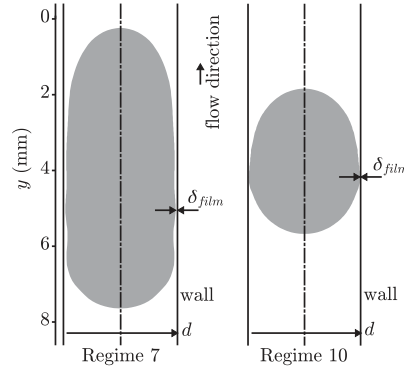
The bubble rise velocity is an important parameter in the understanding of Taylor flow as it impacts mass transfer into the liquid phase. Fig. 5 compares the relative bubble rise velocity, defined by $W = (u_b - u_{tp})/u_b$, where u_{tp} is the two-phase superficial velocity and u_b the bubble velocity, with some of the experimental correlations available in literature. Among available results, the first law $W \sim Ca^{1/2}$, proposed by Fairbrother and Stubbs (1935) is included, which has been shown to be valid up to $Ca = 0.09$ by Taylor (1961). Bretherton (1961) has proposed a different scaling law $W \sim Ca^{2/3}$. More recent correlations are also plotted in Fig. 5, including those of Liu et al. (2005), valid for $2 \times 10^{-4} < Ca < 0.39$, and of Abiev (2013), valid for both small and large Ca , but always low We . Fig. 5 shows that for the regimes in this work, where inertia is not negligible, the values lie between the prediction of correlations of Liu et al. (2005) and Abiev (2013). Note that the value of regime 1 has a larger error bar due to the fact that the flow controllers were operating close to the minimum operating point.

Following Abiev (2008), in the case of slug flow, the local mass conservation equation (continuity equation) can be written for each phase separately and integrated in a cross section of the capillary based on the knowledge of the average surface fraction of each phase; then, an axial integration over one unit cell length in addition to the flow incompressibility condition imposes that

$$u_b A_b + u_{film} A_{film} = u_{tp} A \quad (4)$$



(a) Film thickness experimental measurements compared to correlations from literature



(b) Bubble interface measured by shadowgraphy showing minimum film thickness measurement for regimes 7 and 10 (see table 2 for regime details)

Fig. 6. Experimental liquid film thickness measurements.

where u_{film} is the average velocity in the lubrication film, and A_{film} , A_b and A are respectively the area occupied by the film, the bubble and the whole cross section. This exact balance, Eq. (4), between the different volumetric flow rates can be simplified in the case of a gas-liquid slug flow. Indeed, Howard and Walsh (2013) have shown that the most important parameter playing on the ratio of magnitude between the film and bubble velocities is the viscosity ratio; in the case of gas-liquid flows (very high viscosity ratio), u_{film} can be considered as negligible compared to u_b (assumption of stagnant lubrication film). Moreover, assuming that $Ca \ll 1$ as considered in this study, i.e. $\delta_{film} \ll d$ (see Section 4.2), Eq. (4) is simplified to

$$\frac{u_b}{u_{tp}} \approx \frac{A}{A_b} \approx 1 + \frac{4\delta_{film}}{d} \quad (5)$$

Eq. (5) shows again that the bubble velocity is always larger than the average two-phase flow velocity u_{tp} (or slug velocity), and presents the advantage to emphasise that the relative bubble velocity W and the film thickness are strongly linked in this problem; this is why authors like Howard and Walsh (2013) have proposed an iterative process based on the existing correlations for the estimation of these two flow parameters simultaneously. In the next section, experimental results of the film thickness are compared to existing correlations from the literature.

4.2. Liquid film thickness

Several analyses exist to characterise the thickness of δ_{film} of the lubrication film between the bubble and wall.

Without inertial effects, ($We \ll 1$), in a regime of $Ca \ll 1$, the study of Bretherton (1961), based on the lubrication approximation, shows that δ_{film} is given by the balance of viscous force and the pressure gradient that originates from the difference of curvatures between the spherical bubble cap and the flat region parallel to the wall, which gives the well known law $\frac{\delta_{film}}{d/2} \sim Ca^{\frac{2}{3}}$. This study has been extended by Aussillous and Quéré (2000) for higher values of Ca , but always in visco-capillary regimes under the condition $Ca < 1$, by using a geometric correction on the curvature expression that yields $\frac{\delta_{film}}{d/2} \sim \frac{Ca^{\frac{2}{3}}}{1+Ca^{\frac{2}{3}}}$ where δ_{film} only depends on Ca .

In the presence of inertial effects ($We > 1$), Aussillous and Quéré (2000) have reported that the film thickness increased and they have proposed, in this latter case, a correlation based on both Ca and We . Numerical results of Kreutzer et al. (2005) and Heil (2001) have confirmed the trend and have also taken into account changes in bubble nose curvature through numerical simulations up to $Re_b = 200$. Based on these observations and on extensive measurements of film thickness in gas-liquid flows

by use of a laser focus displacement meter, a new correlation based on a geometric correction was proposed by Han and Shikazono (2009) which takes into account such inertial effects and relates δ_{film} as a function of (Ca, We, Re_b) , even though only 2 of these parameters are independent. The latter correlation has been confirmed by recent measurements of both Howard and Walsh (2013) – based on high speed optical microscopy with refractive index matching which shows an agreement with less than 10% discrepancy, and Kurimoto et al. (2017) – based on high speed camera measurements, showing an agreement between $\pm 20\%$ up to $Re_b = 100$.

The measurements in this work, reported in Fig. 6(a), correspond to the inertial regime and allow for the extension of the comparison with the existing predictive correlations up to $Re_b = 1430$. It should be noted that due to the pointed shaped of some of the bubbles, especially at higher values of Re_b , the liquid film thickness is not always uniform in the flat bubble region and has been defined as the minimum distance between the bubble and the channel wall observed in the shadowgraphy images, as shown in Fig. 6(b). The correlation proposed by Aussillous and Qu er e (2000) compares well with our measurements for regimes $We < 1$, with an average difference of 15.8%. In contrast, for regimes 5–9 which correspond to the highest We (ranging from 3.2 to 10.6), the prediction of film thickness by the correlation of Han and Shikazono (2009) that does consider inertial effects is clearly improved. It can be observed that the experimental measurements are in very good agreement with the correlation of Han and Shikazono (2009) for all the fluids considered here, with an average difference of 16.0%, despite a maximum difference of 47% for regime 5.

4.3. Time-averaged velocity fields in slugs

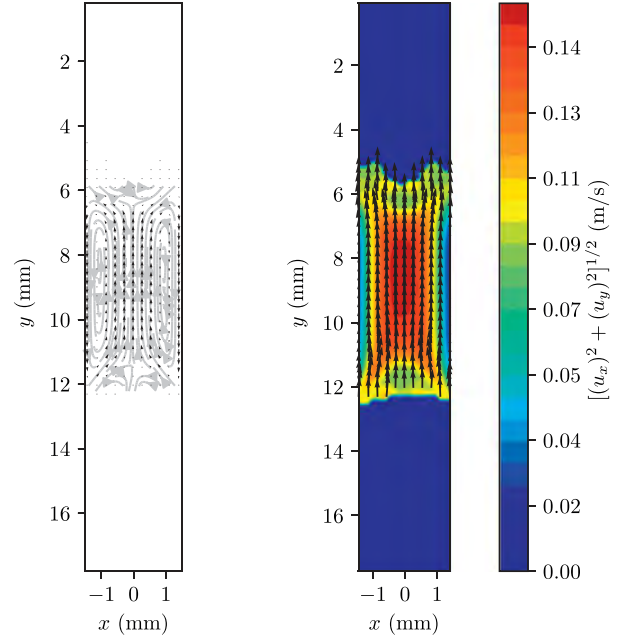
The value of W , the relative bubble velocity, is directly related to the flow streamlines, as shown by Taylor (1961). For values of $Ca < 0.7$ and $W < 0.5$ as for all regimes in the present work, the flow patterns consist of a recirculating flow in the liquid slug, with stagnation points existing on the bubble nose. This flow organisation is visualised by calculating the time-averaged velocity field using the PIV technique, and by subtracting the bubble velocity from the time-averaged velocity u_{tp} previously calculated, to obtain the mean velocity field in the bubble reference frame. Fig. 7(a) shows this mean velocity field for flow regime 2 superimposed with streamlines. Two mirrored recirculation flow patterns are observed and compared well to the concentration patterns obtained by PLIF-I technique for the same flow regime (see Fig. 9).

For regime 2, a radial velocity profile, calculated in the fixed reference frame is also presented in Fig. 8. This mean velocity profile, extracted at halfway along the slug length, is well fitted by a parabola, which is consistent with the Poiseuille flow model usually found when the slug length is greater than a few diameters (Thulasidas et al., 1997). As a consequence the flow in the liquid slug can be considered to be fully developed for this regime.

4.4. Time-averaged O_2 concentration fields

The time-averaged O_2 concentration fields measured using the PLIF-I technique for the 14 different regimes are presented in Fig. 9. For each regime, the contours close to the inlet, at a distance z_1 , and then at the second field of view, z_2 , are presented. The half unit cells extracted during the image processing are mirrored about the axial centreline as one half of the liquid slug is partially hidden by the bubble shadow (see Fig. 4(h) and (i)), and as each unit cell is observed to be axisymmetric.

A wide variety of hydrodynamic regimes have been explored, where the concentration fields can be seen to vary significantly.



(a) velocity vectors and streamlines in slug reference frame. (b) velocity vectors and magnitude in fixed reference frame.

Fig. 7. Experimental PIV time-averaged velocity fields for regime 2 (see Table 2 for regime details).

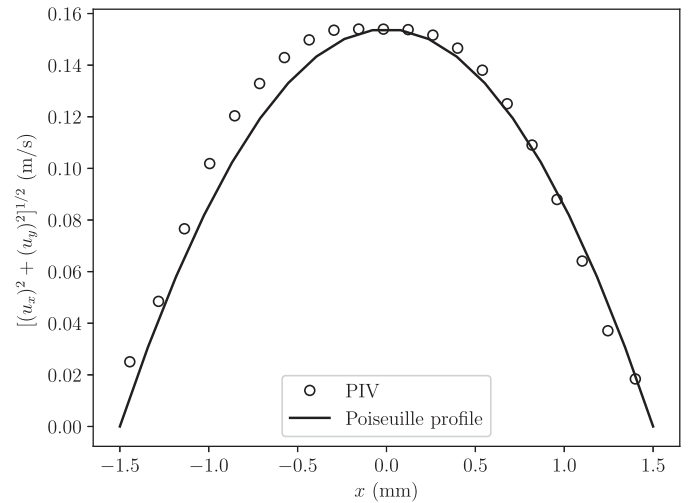
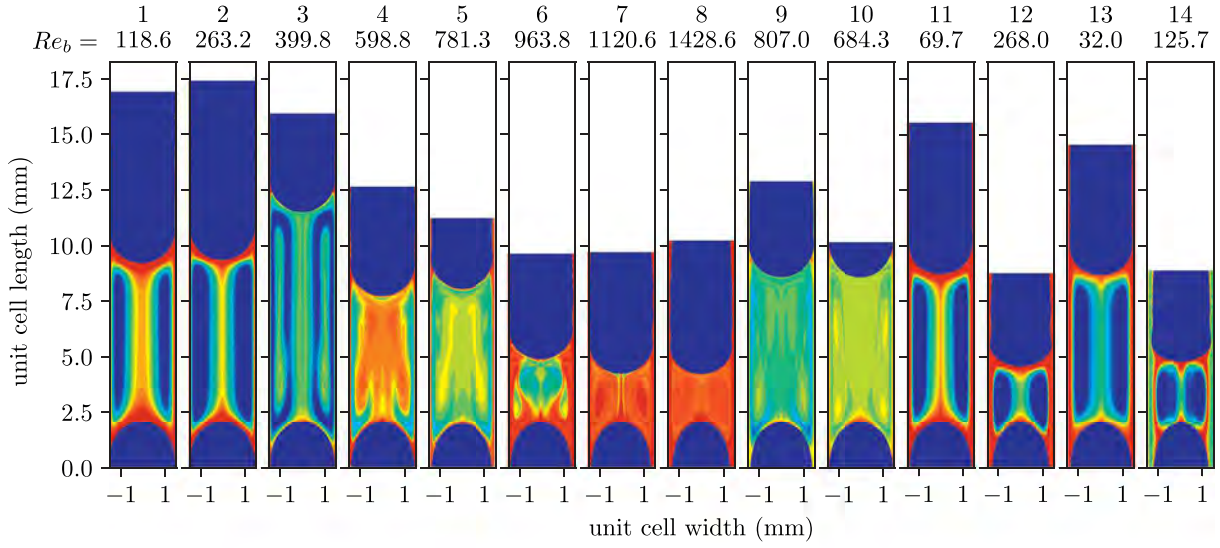
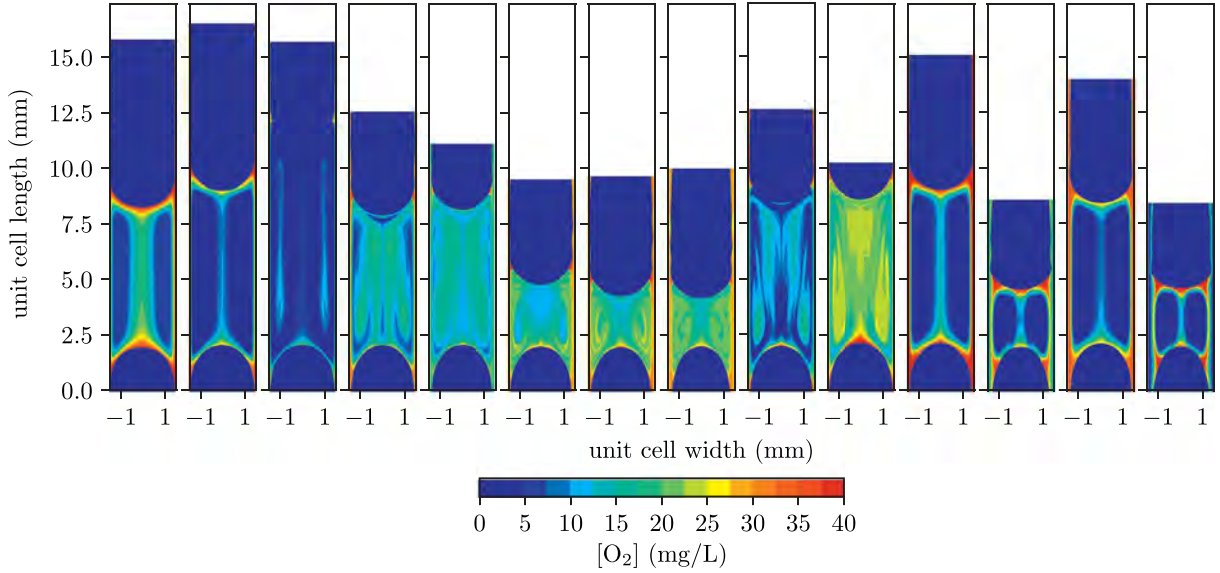


Fig. 8. Radial velocity profile in the fixed reference frame for regime 2 extracted halfway along the slug length.

Some zones can be generally distinguished. Firstly, in liquid slugs, there is a recirculation pattern, as mentioned previously, which ensures transport of O_2 between the two consecutive bubbles of the train (see for example regimes 1, 2, 11, 13 in Fig. 9). Then, along the tube axial centreline, a region with a higher concentration than the rest of the slug is generally visible. This is explained by the existence of a maximum in velocity at the channel centreline, making convective transport of O_2 the most efficient, with a relative velocity equal to $2u_{tp} - u_b$ when considering an established Poiseuille flow in the slug. Finally, along the channel wall, the resolution of the experimental measurements allows for the observation of a thin concentration film: this film is associated with the lubrication film between the flat region of the bubble and the wall, but also extends along the channel wall in the unit cell. In



(a) Axial distance z_2 from inlet



(b) Axial distance z_1 from inlet

Fig. 9. Time-averaged and normalised O_2 concentration contour plots. These images have been corrected for scattered light and radial distortion. The half unit cells are mirrored about the axial centreline. The $[O_2]$ values inside the bubble have been set to 0 for clarity.

this way, for the mass transport analysis, a continuous film along the channel wall is considered, lying between the radial position of the dividing streamline in the slug and the wall, as shown in Fig. 10. This dividing streamline, illustrated by Taylor (1961) and Thulasidas et al. (1997), is the streamline connecting the stagnation points on the front and rear of the bubble surface, which thus separates the circulating vortex in the slug from the liquid film attached to the wall. Assuming a Poiseuille flow in the slug, the radial position r_1 of the dividing streamline (Thulasidas et al., 1997) can be predicted by

$$r_1 = \frac{d}{2} \sqrt{2 - \frac{u_b}{u_{tp}}} \quad (6)$$

This stagnant film is rich in O_2 all along the channel wall because of both radial diffusion in the lubrication film in contact with the bubble and efficient axial convective transport in the vicinity of the

sliding interface, due to the relative velocity between the bubble and the lubrication film, which is close to u_b , when considering a stagnant film.

As the flow travels from z_1 to z_2 , the $[O_2]$ increases in the different regions. The liquid can be seen to approach saturation at z_2 for regimes 7 and 8 which are the regimes at highest Re_b . For the regimes of 10% Breox (13 and 14) at the highest Ca , the increase in $[O_2]$ in the liquid film can be clearly observed because of the relatively larger film thickness when compared to the other regimes.

Regimes 1 and 2 for water, and 11–14 with Breox, show concentration fields similar to what is observed in some numerical studies for cases of physical absorption, such as in Shao et al. (2010) and Hassanvand and Hashemabadi (2012), with the centre of the vortex being the point in the slug which is fed the slowest with O_2 since diffusion has to transfer O_2 across the recirculation streamlines.

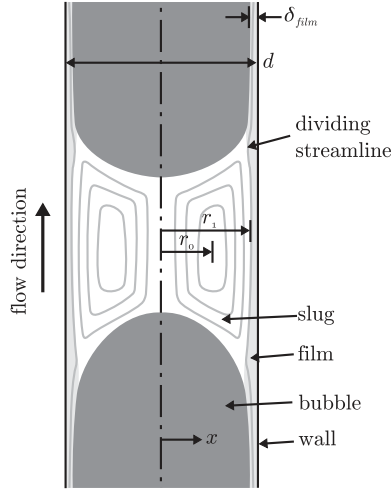


Fig. 10. Sketch showing the different characteristic dimensions and areas in the unit cell.

Nevertheless, for regimes 3–10, an interesting feature which appears is the presence of vortices of uncharacteristic concentration levels in the slug, described as an area of relatively high concentration in the centre of the slug surrounded by a zone of lower concentration, which is clearly visible for regime 3, 7 and 8 for example. It is worth reminding here that these Taylor flow regimes are not associated with oscillations of the bubble nose and that, even though $[O_2]$ fields presented in Fig. 9 are time-averaged, the instantaneous fields have the same structure and do not show large fluctuations in the concentration values. A possible explanation for these features is that they are associated with particular flow dynamics, different from that shown in Fig. 7, which appears after a critical value of about $Re_b > 300$. This will be discussed later. Because of the strong impact of hydrodynamics in the slug on the concentration fields, in the following sections, the local transfer mechanisms are first described for cases of classical concentration fields like those observed at $Re_b < 300$, and cases associated to anomalous patterns at $Re_b > 300$ are discussed separately.

4.5. Analysis of local mechanisms for mass transfer at $Re_b < 300$

Here the mass transfer dynamics for regimes 1–2 and 11–14, for which $Re_b < 300$, are analysed. The flow structure is well known in the literature and is similar to that presented in Section 4.3. It induces concentration fields for which the dynamics of the different regions (film and slug) can be distinguished.

Firstly, profiles of $[O_2]$ along the normal direction to the interface are considered. They are extracted at the bubble nose at the radial position of $x/2$. From these profiles, we choose a criterion to evaluate the boundary layer thickness: we extract the distance n in the normal direction from the bubble surface where $[O_2](n) = 0.4C^*$, for the two residence times $t_1 = \frac{z_1}{\bar{u}_b}$ and $t_2 = \frac{z_2}{\bar{u}_b}$. The result is shown in Fig. 11 where the temporal evolution of the boundary layer thickness at this point is plotted. Note that even though the values of concentration in the vicinity of the interface are not reliable at very short distances due to the spatial resolution of the measurements (i.e. 1 pixel $\sim 7 \mu\text{m}$), at distances greater than $d/30$, which is the minimum boundary layer thickness measured here, concentration values are accurate. This is a distinct advantage of the experimental measurements compared to direct numerical simulations with coarser meshes, which do not adequately resolve the boundary layers at short time (when they are the thinnest), and will then not be able to accurately reproduce the total mass transfer dynamics (Gupta et al., 2009).

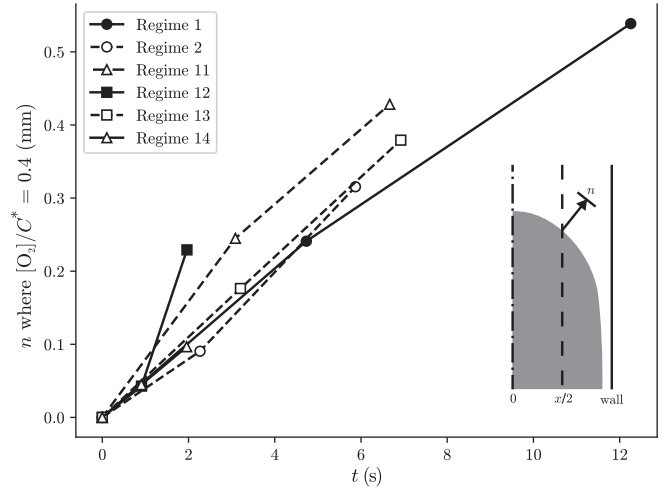


Fig. 11. Evolution of the $[O_2]/C^* = 0.4$ layer thickness normal to the bubble interface.

For these regimes, it can be observed in Fig. 11 that the boundary layers evolve almost linearly over time, or even faster for regime 12, which reflects the enhancement of transfer due to the recirculation patterns in the slugs compared to a purely diffusive case, which would correspond to an evolution as the square root of time. Surprisingly, it can be seen in Fig. 11 that comparable rates of evolution of these layer thicknesses at these points are found for all regimes, despite different magnitudes of recirculation velocities in the slugs. The impact of these recirculation velocities will be more noticeably visible when analysing the average slug concentration dynamics.

Now the examination of temporal evolution of radial concentration profiles both behind the bubble and at mid-length of the slug emphasises the role of the film along the channel wall in the mass transfer process. As a reminder, the film region for mass transfer analysis is defined all along the channel wall: next to the bubble, it corresponds to the lubrication film and in the slug area, it is the region lying between the radial position of the dividing streamline r_1 and the channel wall. Among all cases considered in this section, two configurations can be distinguished based on the concentration profile in the film: this is illustrated in Fig. 12 by presenting the radial profiles recorded at times t_1 and t_2 for regimes 1 and 14. Regime 1 is representative of a case of a thin lubrication film (small Ca) like regimes 2, 11 and 13, whereas regime 14 corresponds to a thicker film (higher Ca) which has dynamics similar to regime 12.

In the case of regime 1, the film is the region the most concentrated in O_2 , showing a concentration level even higher than that observed in the slug region next to the axis of symmetry ($x = 0$). The maximum concentration area seems to be close to the wall, under the limit of the resolution of the experimental setup in the film region (probably insufficient at t_1 because the thin zone with a zero concentration gradient at the wall is not visible at this instant, contrary to t_2), which leads to the belief that the first and major source of oxygen corresponds to a zone where the interface is the closest to the wall, at the point where the lubrication film thickness should be the minimum. Then, the film becomes rapidly saturated in O_2 with a clear homogenisation in concentration between positions z_1 and z_2 , due to the combination of rapid diffusion through the thin film adjacent to the bubble and efficient convective transport by the sliding velocity between the film and the bubble. Consequently, for this case, the film rapidly becomes another source of O_2 for the slug region, in addition to the bub-

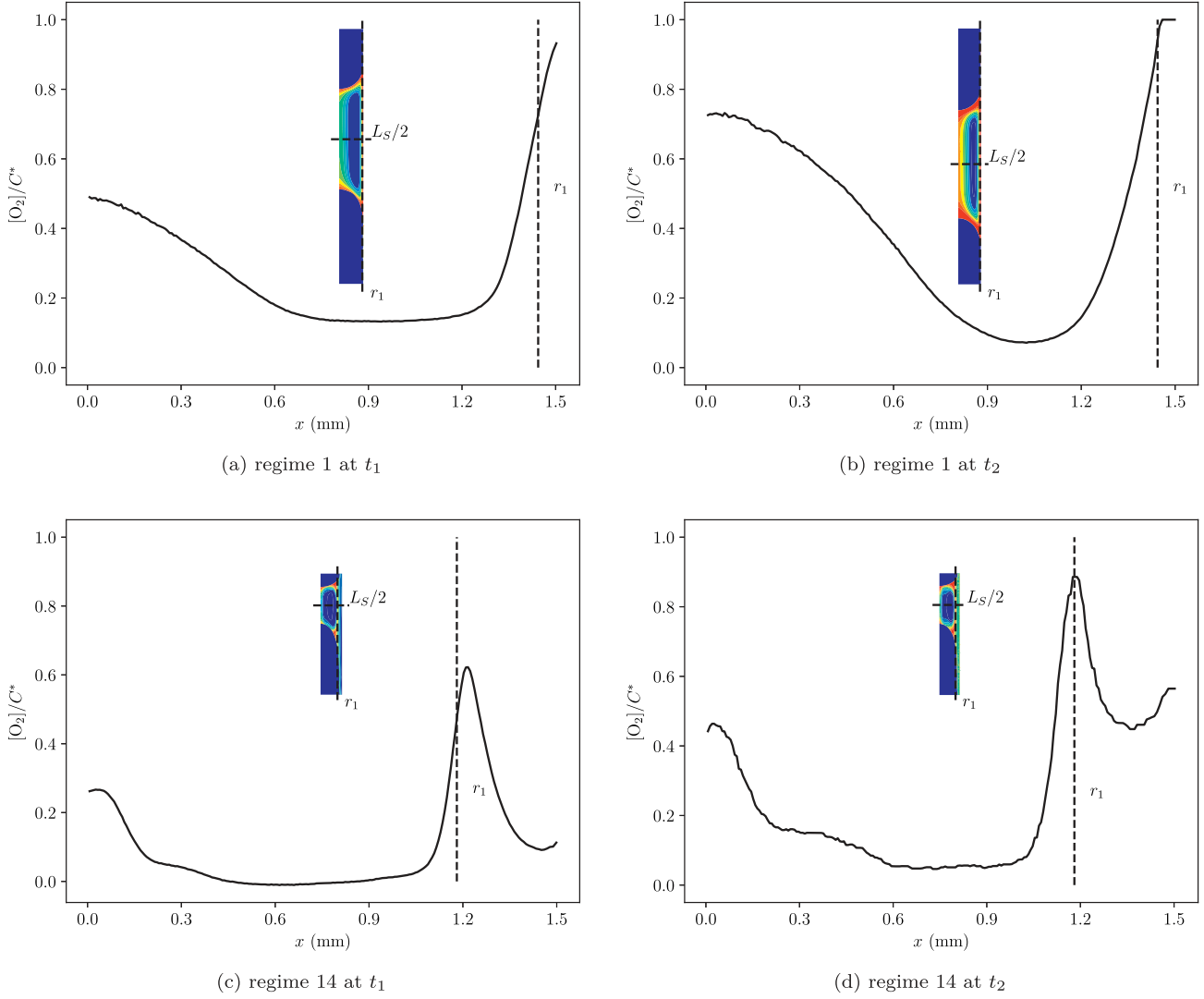


Fig. 12. Radial profiles of $[O_2]/C^*$ in the centre of the slug from $x = 0$ to 1.5 mm with the corresponding concentration field inset.

ble interface directly in contact with the slug. In particular, data extracted from the concentration profiles of Fig. 12 show that the concentration gradient in the radial direction at the position of the dividing streamline – which represents the rate of mass transfer between the film and the centre of the slug – is 10 times higher than the corresponding radial gradient observed in the vicinity of the symmetry axis – which represents the rate of mass transfer between the region near the axis and the centre of the slug. For modelling purposes, if one decides to separate the whole liquid into a slug region and a film region, it is thus compulsory to include a rate of mass transfer between the film and slug (Butler et al., 2016).

In the case of regime 14 (see Fig. 12(c) and (d)), access to earlier stages of the mass transfer dynamics is possible because the diffusion process is slower compared to regimes 1 and 2 due to a lower diffusion coefficient in the water-Breox solutions. Note that concentration profile very close to the wall is again not totally well captured at t_1 because the zero gradient area of the concentration field at the wall is not accurately described. However the high resolution of this technique associated with a large lubrication film in this case allows us to obtain a sufficiently good description of the concentration field in the film. It can be observed that the profile is totally different to the previous case since it presents a local maximum at the position of the dividing streamline, corresponding therefore to a filament of dissolved O_2 coming from the bubble,

visible in Fig. 12(c). This filament feeds both the slug region and the rest of the film, with comparable rates of mass transfer at each side of r_1 . Contrary to the previous case, the film is very heterogeneous in concentration with a non-monotonous profile in the radial direction, and we notice for instant t_2 (see Fig. 12(c)) the presence of another local maximum close to the wall, which raises the question of an additional source of O_2 diffusion coming from an interface point very close to the wall. These two sources contribute to the increase in the film concentration over time. Therefore, the dynamics in the film are more complex for these regions of large Ca and low mass diffusivity (14 and 12). Finally, the two different dynamics observed here concerning the role played by the film in the transfer dynamics originate from different film thicknesses, but also probably from local differences of curvatures of the bubble shapes. It could then be informative to complete these observations through numerical studies that could provide evidence of the feeding points for the diffusion process and the influence of interface shapes.

To provide guidance for the estimation of the mass transfer between the film and slug areas, the diffusive rate has been calculated from the PLIF-I concentration fields by

$$\varphi_{film-s} = -D \left[\frac{\partial [O_2]}{\partial x} \right]_{x=r_1} \quad (7)$$

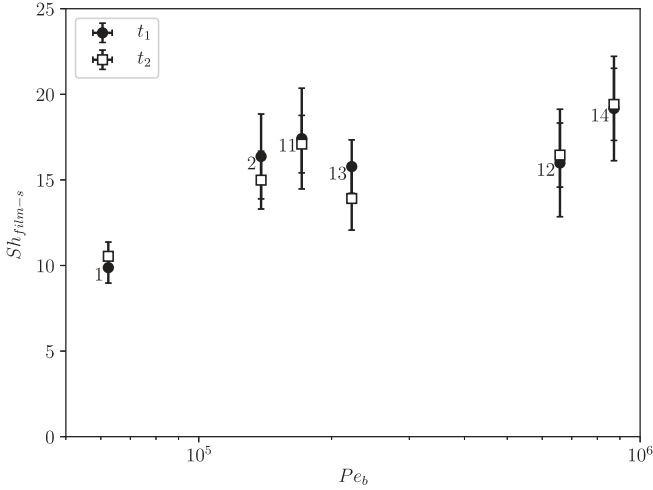


Fig. 13. Local Sherwood number for the estimation of the mass transfer rate between film and slug, determined at instants t_1 and t_2 for regimes 1, 2, and 11–14.

and a local Sherwood number has been defined as

$$Sh_{film-s} = \frac{d[\partial[O_2]/\partial x]_{x=r_1}}{C^*} \quad (8)$$

Fig. 13 shows Sh_{film-s} measured at the two instants t_1 and t_2 for these six regimes as a function of the Pelet number $Pe_b = \frac{u_b d}{D}$, defined by using the sliding velocity in the lubrication film, which is close to u_b . It is observed that this local Sherwood number remains nearly constant, ranging from 10 to 20, and presents a very low dependency on Pe_b even though the latter varies by more than one order of magnitude.

4.6. Transition to regimes at $Re_b > 300$

With values of $Re_b > 300$, which is the case for regimes 3–10, other features appear in the concentration fields which cannot be explained by a dynamic similar to what has been described at lower Re_b . This transition occurs between regimes 2 and 3. In particular, the presence of local maxima of concentration in the centre of the slug, such as in regime 3, can be observed and some coherent structures of specific concentration levels are clearly visible for regimes 4–10. As a reminder, these structures are also visible on the instantaneous PLIF-I images. To our knowledge, such features in concentration fields have not been reported in literature so far, neither in experimental nor in numerical works.

Several hypotheses can be claimed to explain these observations. Firstly, this phenomenon could originate from particular hydrodynamics close to the T-mixer, in a similar way to what was observed by Yang et al. (2016) who found that the injection zone is responsible for a significant proportion of the overall mass transfer. Moreover, the structures of concentration contours, which are visible on the average fields for regimes at $Re_b > 300$, also lead to the belief that a flow instability could appear at sufficiently high Re_b and produce vortices in the slug and/or fluctuations of low intensity. Such an instability may come up in the bubble wake due to the presence of impurities like surfactants adsorbed at the bubble surface, therefore giving a solid-like behaviour to the interface at the rear of the Taylor bubble. Indeed, it is known that in the case of an unconfined flow past a solid particle, the sphere wake remains steady and axisymmetric provided that the Reynolds number is lower than 200. Above this value however, axisymmetry first vanishes for Reynolds numbers between 210 and 270, and unsteady flows are observed for larger Reynolds numbers (Johnson and Pattel, 1999). Thus, wake instability in such

a flow appears at Reynolds numbers comparable to the value of 300 that is observed here to be critical in (confined) Taylor flow, which supports this assumption of the result of interface contamination. To date and to the best of our knowledge, the only work where a Taylor flow image of the concentration field is visible is Kastens et al. (2017) where a single Taylor bubble is studied by the PLIF-I technique for Sh in the range 200–2000. They suggest surfactants as a possible cause to anomalous concentration distribution and highlight the fact that, in this type of experiment, a perfectly clean system is nearly impossible to achieve under realistic conditions.

On the PIV images of the present work, even if non-axisymmetric features are not observed in the slug when $Re_b > 300$, the PIV measurements reveal flow unsteadiness. Around the critical value for Re_b , for the two flow regimes 2 and 3, characterised, respectively, by $Re_b = 260$ and $Re_b = 400$, the fluctuating velocity fields have been calculated. Fig. 14(a) shows that velocity fluctuations along the axis of symmetry at $x = 0$ reach several percents of the bubble velocity. We precise that the uncertainty of the velocity fluctuations have been quantified following Sciacchitano and Wieneke (2016), and remains much lower than the observed fluctuations, in the range of 0.2% of u_b . Higher fluctuations can be noticed in the axial region for regime 3 compared to regime 2, with maximum values localised near the rear of the bubble. These fluctuations decrease in intensity up to the nose of the following bubble. This observation tends to confirm the existence of an instability produced in the bubble wake, and associated with fluctuations of about 4% of u_b (for regime 3), even though the velocity field issued from PIV analysis for regime 3 does not reveal any coherent structure in the bubble wake. Subsequently, consequences are visible on the mass transfer dynamics for these regimes. If we compare the mean concentration fields of regimes 2 and 3 in Fig. 9, focusing close to the axis between the bubble nose and tail, we notice a thin zone of high concentration for regime 2, which is richer than that observed in regime 3, the latter being also wider in the axial region. By further comparing the longitudinal concentration profiles along the axis in Fig. 14(b), regime 2 exhibits symmetry of the concentration profile, with a horizontal axis passing halfway through the slug, while for regime 3, symmetry is broken and O_2 concentration is increasing from the rear of the bubble to the nose of the following one. In this latter case, this suggests that the velocity fluctuations close to the rear of the bubble enhance mixing and modify the topology of the concentration field compared to stable regimes at $Re_b < 300$. For regimes 4–10, the structure of the concentration field in the slug is modified even further than that of regime 3.

Note that, for all these disturbed regimes, the concentration field in the film region does not show spatial heterogeneities, as compared to those observed in the slug. The film is always more concentrated than the rest of the slug, meaning it remains, as well as the bubble interface, a source of O_2 that feeds the inner slug.

In the following section, despite the presence of perturbed patterns of concentration in the slugs for regimes 3–10 due to a possible wake instability, an attempt to relate the global mass transfer dynamics to the intensity of the recirculation motion in the slug, for all the studied regimes, is performed.

4.7. Global mass transfer dynamics and scaling law

4.7.1. Mass transfer dynamics

For all regimes, 4 values of local normalised liquid concentration $C(z)/C^*$ are known: the values at inlet and outlet of the tube section were measured by the O_2 sensor, and the values obtained by spatial averaging of the local concentration field from the PLIF-I images acquired at the two axial positions z_1 and z_2 . They can be expressed as instantaneous values of concentration in the unit

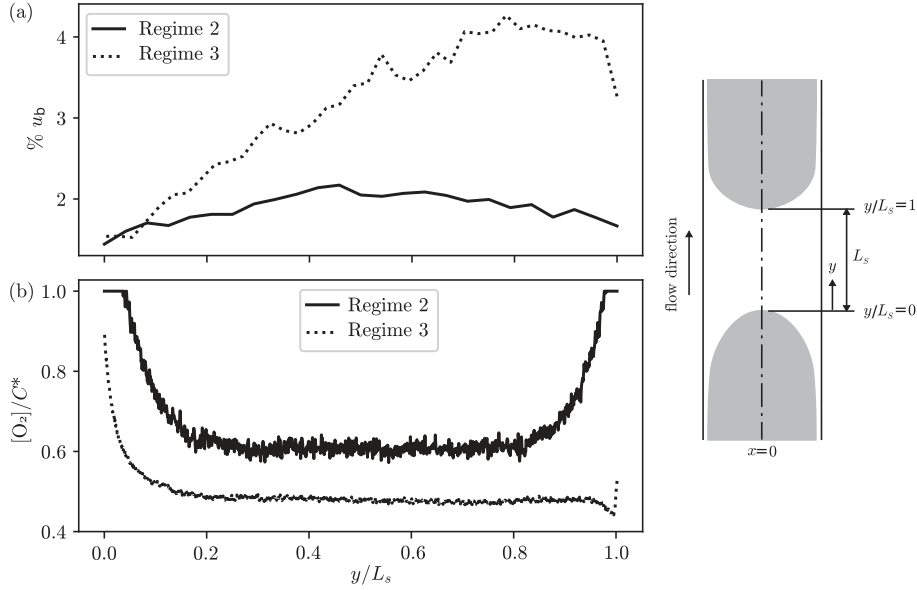


Fig. 14. Axial profiles at $x = 0$ for regimes 2 and 3 (a) relative bubble velocity fluctuation, (b) normalised oxygen concentration.

cell $C(t)/C^*$ by using the bubble residence time, defined as $t = \frac{z}{u_b}$. From the four measured points, the mass transfer dynamics can be quantified. It is noted here that the notation for concentration C differs from $[O_2]$ used previously, as the latter refers to the oxygen concentration values in the concentration field, while the former refers to the volumetric average oxygen concentration in the liquid phase, calculated in a manner similar to Eq. (3).

The simplest model based on one global transfer coefficient k_L , assumed constant, writes the instantaneous rate of mass transfer as

$$\varphi_{uc}(t) = Vol_{uc} \frac{dC}{dt} = k_L a Vol_{uc} [C^* - C(t)] \quad (9)$$

where a is the gas-liquid interfacial area per unit cell volume which is known for each regime from processing of the shadow-graph images. The solution of Eq. (9) predicts a temporal evolution in the form

$$C(t)/C^* = 1 - e^{-k_L a t} \quad (10)$$

This model is referred to as the plug flow model, corresponding to an assumption of uniformity of velocity and concentration in each unit cell of the Taylor flow, and it is associated to the volumetric mass transfer coefficient $k_L a$. Fig. 15 compares the experimental measurements for each regime with this model where the $k_L a$ values have been chosen by least-squares fitting. It shows that the plug flow prediction quite accurately describes the transfer dynamics for most regimes, with the worst fits being regimes 4, 5, 11 and 13 for which the dynamics are slightly underestimated. For these cases, a global 1st order model cannot accurately predict the actual decrease of mass transfer rate between the two phases which is observed after a certain time (Butler et al., 2016). Nevertheless, it can be considered sufficient, as a first approximation, to use a model with one adjustable parameter k_L because only four instantaneous experimental values of concentration are available for each regime. Note that $k_L a$ value reaches up to 2.46 s^{-1} , associated to a Sherwood number of 4000 (regime 8).

4.7.2. Scaling law for the overall mass transfer in Taylor flow

The transfer dynamics can then be compared between the different regimes by defining a global Sherwood number as $Sh = \frac{k_L d}{D}$. *A priori*, the mass transfer dynamics could depend on the independent non-dimensional numbers of the problem, i.e. (Re_b , Sc , We). In

the concentration fields, the film zone represents a volume of only 10% of Vol_{uc} at maximum (in cases of larger lubrication films). The evolution of the average liquid concentration is therefore mainly controlled by the concentration reached in the slug, keeping in mind the role of the film in the transfer process as a complementary source of dissolved O_2 for the slug. In the slug, if we assume a Poiseuille flow, without considering the presence of any temporal fluctuations, the velocity which ensures mass transfer corresponds to the velocity of the liquid relative to the bubble, no matter if the Taylor flow is ascending or descending, with a profile given by

$$u(x) = 2u_{tp} \left[1 - 4 \left(\frac{x}{d} \right)^2 \right] - u_b \quad (11)$$

This profile describes a recirculation motion in the slug, with a radial position $r_0 = \frac{d}{2\sqrt{2}} \sqrt{2 - \frac{u_b}{u_{tp}}}$ where velocity vanishes (see Fig. 10). From this, following Thulasidas et al. (1997), the average recirculation velocity in the vortex can be calculated based on the time t_{cir} required to displace liquid from the rear of one bubble to the nose of the following one in the train (i.e. along one slug length L_s),

$$u_{cir} = \frac{L_s}{t_{cir}} \quad (12)$$

with

$$t_{cir} = \frac{\pi L_s r_0^2}{2\pi \int_0^{r_0} u(x) x dx} = \frac{L_s}{2u_{tp} - 4u_{tp} \left(\frac{r_0}{d} \right)^2 - u_b} \quad (13)$$

Finally, the recirculation velocity in the capillary tube is given by

$$u_{cir} = 2u_{tp} - 4u_{tp} \left(\frac{r_0}{d} \right)^2 - u_b \quad (14)$$

Note that, using the expression of r_0 , it can be found that $u_{cir} = u_{tp} - \frac{1}{2}u_b$. From Eq. (14), a recirculation Reynolds number can be defined as $Re_{cir} = \frac{\rho_L u_{cir} d}{\mu_L}$. Re_{cir} is expected to have a strong influence on the mass transfer because, in the slug, diffusion is ensured across the streamlines of the recirculation motion, with sources of O_2 coming from (i) the nearly spherical rear of a bubble, (ii) the nearly spherical nose of the following bubble and (iii) the film which is more concentrated than the slug.

At a given value of Schmidt number, i.e. for all water regimes 1 to 10 at $Sc = 526$, Sh as a function of Re_{cir} is plotted in Fig. 16.

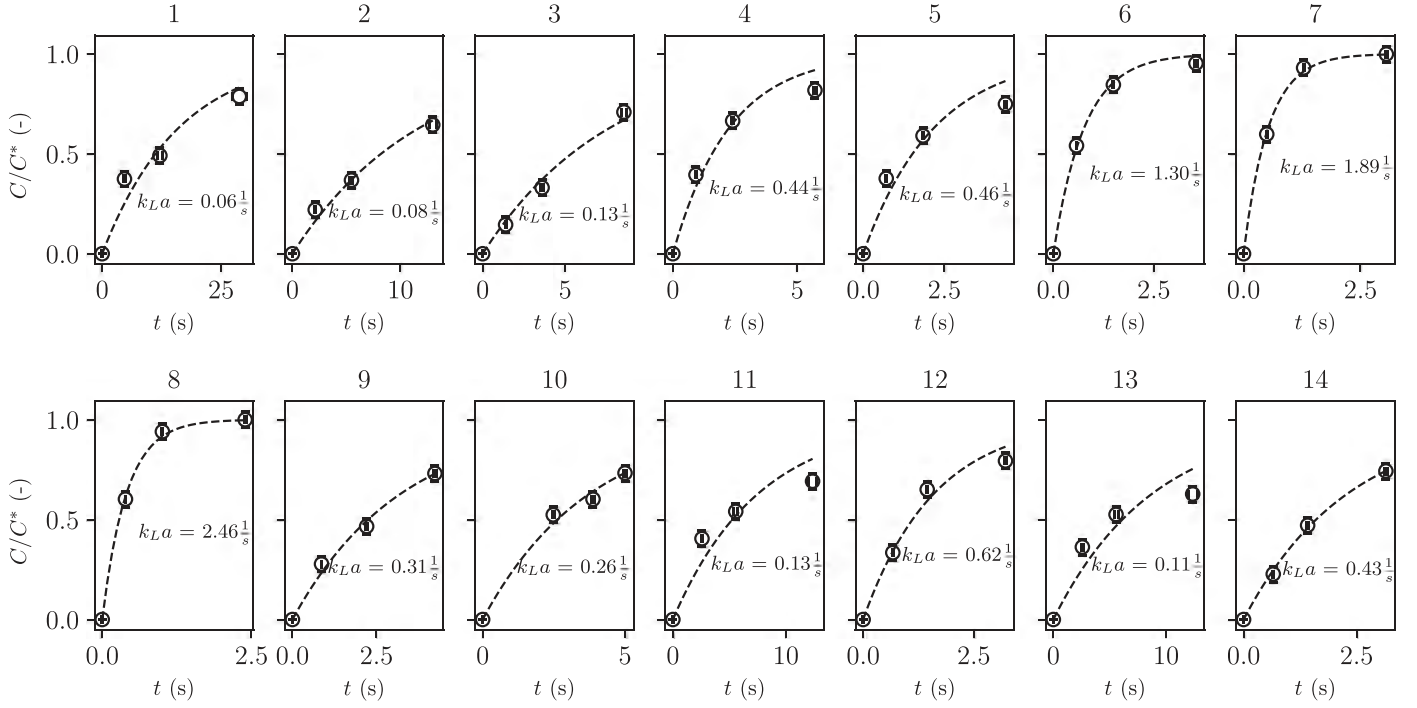


Fig. 15. Evolution of $C(t)/C^*$ in the overall liquid phase (slug + film) along the channel (as $t = \frac{z}{u_b}$) for all regimes showing the experimental points and the fitted plug flow model of Eq. (10).

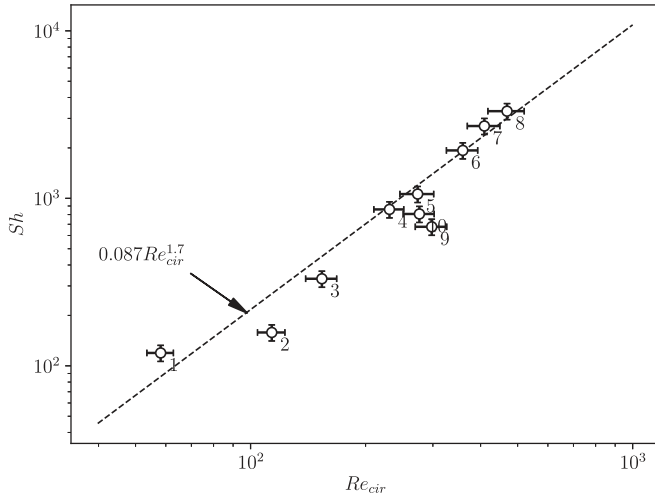


Fig. 16. Re_{cir} vs Sh for all water regimes at $Sc = 526$.

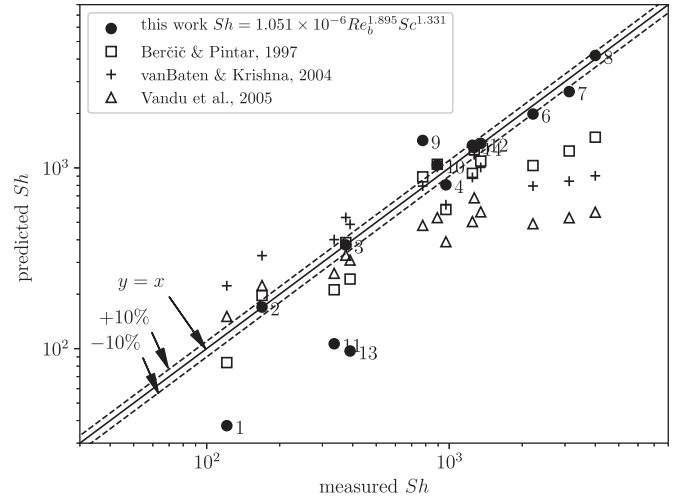


Fig. 17. Comparison of Eq. (15) to available scaling laws from literature.

It can be seen that all points lie on a single curve, demonstrating the importance of the intensity of the recirculation motion in the transfer dynamics. This slight discrepancy of this power law may result from the large variations of We (over two orders of magnitude) for all these regimes; however, Re_{cir} is clearly the most important parameter which gives Sh at a given Sc .

With the objective to produce a simple predictive correlation for the mass transfer coefficient for all regimes studied in the present article, which relies on an interpretation of the transfer dynamics by a plug flow model with constant mass transfer coefficient, the choice is made to consider as a first approximation that $u_b \approx u_{tp}$, which results in $Re_{cir} \approx \frac{1}{2}Re_b$. It is then proposed to relate Sh as a function of both Re_b and Sc . In this way, the final scaling law is then

$$Sh = 1.051 \times 10^{-6} Re_b^{1.895} Sc^{1.331} \quad (15)$$

Table 3

Scaling laws from literature chosen as reference for the present work.

Reference	Correlation
Berčić and Pintar (1997)	$Sh = \frac{d}{aD} 0.111 \frac{u_{ip}^{1.89}}{[(1-\varepsilon_g)L_{uc}]^{0.57}} \sqrt{\frac{D}{D_{CH_4}}}$
Van Baten and Krishna (2004)	$Sh = \frac{d}{aD} \left(\frac{2\sqrt{2}}{\pi} \sqrt{\frac{Du_b}{d}} \frac{A}{L_{uc}} + \frac{2}{\sqrt{\pi}} \sqrt{\frac{Du_b}{\varepsilon_g L_{uc}}} \frac{4\varepsilon_g}{d} \right)$
Vandu et al. (2005)	$Sh = \frac{d}{aD} 4.5 \sqrt{\frac{Du_b}{L_{uc}}} \frac{1}{d}$

Note that exponent of Re_b is nearly the same as that of Re_{cir} in the power law function in Fig. 16, and that the use of We in this proposed correlation does not help in improving its accuracy.

This scaling law is compared in Fig. 17 to well known scaling laws available in literature (see Table 3) which are de-

rived from experimental works (Berčić and Pintar, 1997; Vandu et al., 2005) or from numerical studies (Van Baten and Krishna, 2004) performed with circular capillaries. It is worth mentioning that the experiments derived by Berčić and Pintar (1997) and Vandu et al. (2005) were restricted to Re_b values lower than 600 and 2000 (respectively), and that the numerical study from Van Baten and Krishna (2004) satisfactorily compared to the data acquired by Vandu et al. (2005).

According to Fig. 17, Eq. (15) satisfactorily gathers the experimental data acquired in the present work for all regimes except 1, 11 and 13 ($Re_b > 120$), within $\pm 11\%$ in most cases. The various scaling laws which are also presented in Fig. 17 provide the same order of magnitude for the Sherwood number when $Sh < 500$. However, they fail in the prediction of Sh when $Sh > 1000$, and show a significant underestimation of Sh for $Sh > 2000$ (regimes 6–8 with the highest Sh), which correspond to a range that the cited works did not investigate.

5. Conclusions

In this work we have studied the hydrodynamics and mass transfer in gas–liquid Taylor flow at bubble and slug scale with high resolution non-invasive techniques, for the case of physical absorption. Both ascending and descending con-current flows have been considered at $Ca \ll 1$ and moderate to high Reynolds number, $Re_b \mathcal{O}(10 - 1000)$, which includes experiments where the Weber number varies over two orders of magnitude $\mathcal{O}(0.1 - 10)$. Mass transfer has been studied at various Sc by changing the liquid phase, using tap water and water-Breox solutions.

Concerning hydrodynamics, in the case of gas–liquid Taylor flows, the lubrication film between the bubble and wall can be considered stagnant. Then, the ratio u_b/u_{tp} of the bubble velocity compared to the total superficial velocity is directly related to the normalised film thickness δ_{film}/d . For all regimes considered here that cover a large range of We , our results confirm that this thickness can be accurately predicted by the correlation of Han and Shikazono (2009) which includes inertial corrections compared to previous correlations, with a precision of $\pm 16\%$ up to $Re_b = 1300$.

Concerning mass transfer, the combined analyses of the results have allowed us to present evidence of the local mechanisms responsible for oxygen transfer. These analyses have enabled the distinction of the contribution of the slug, dominant in volume, and that of the film, which corresponds to the extension of the lubrication film next to the bubble all along the channel wall (which is separated from the slug by a dividing streamline) and which is a region rapidly enriched in oxygen. It has been seen that even though the global mass transfer in the liquid is mainly driven by the rate of transfer towards the slug, the film contribution is important since it acts as a source of oxygen that feeds the slug, in addition to the bubble interface directly in contact with the slug region.

Two contrasted regimes have been highlighted for the first time, depending on a critical Re_b of 300 in which the distribution of dissolved gas concentration among the slug is fairly different. The assumption of the presence of impurities adsorbed at the bubble interface is proposed to explain such hydrodynamic perturbations. Though no unsteady coherent structures of small scale could be observed in the slug in addition to the large recirculations of the average flow, temporal velocity fluctuations were put in evidence, that are localised at the rear of the bubble and that tend to increase mixing for all cases at $Re_b > 300$. Despite these contrasted regimes, the global mass transfer dynamics are controlled in both cases by the concentration level in the slug, which gives a crucial importance to the recirculation motion between 2 bubbles. The conventional 1-d dimensional analysis of the overall mass transfer along the Taylor flow allows for the consideration of a scaling

law for the Sherwood number relative to Re_b and Sc parameters. Laws available in literature and built either from experimental or numerical works have been tested and could not accurately predict the present experimental data. A new scaling law has been derived which satisfactorily gathers experimental results with an average accuracy of $\pm 11\%$ provided $Re_b > 120$, which is better than the existing correlations in that range.

As prospective work and to further understand the fine scale phenomena involved in Taylor flow at high Re_b , a CFD study is in progress.

Acknowledgements

The authors thank the Agence Nationale de la Recherche (ANR) for financial support, the research federation FERMaT for financial and technical support, and F. Xu and N. Dietrich at the LISBP laboratory (INSA, Toulouse, France) for measurement of mass diffusivities of oxygen in water-Breox solutions.

Supplementary material

Supplementary material associated with this article can be found, in the online version, at doi:[10.1016/j.ijmultiphaseflow.2018.04.005](https://doi.org/10.1016/j.ijmultiphaseflow.2018.04.005).

References

- Abiev, R.S., 2008. Simulation of the slug flow of a gas–liquid system in capillaries. *Theor. Found. Chem. Eng.* 42 (2), 115–127.
- Abiev, R.S., 2013. Bubbles velocity, Taylor circulation rate and mass transfer model for slug flow in milli- and microchannels. *Chem. Eng. J.* 227, 66–79.
- Aussillous, P., Quéré, D., 2000. Quick deposition of a fluid on the wall of a tube. *Phys. Fluids* 12 (10), 2367–2371.
- Berčić, G., Pintar, A., 1997. The role of gas bubbles and liquid slug lengths on mass transport in the Taylor flow through capillaries. *Chem. Eng. Sci.* 52 (21–22), 3709–3719.
- Bretherton, F.P., 1961. The motion of long bubbles in tubes. *J. Fluid Mech.* 10 (2), 166–188.
- Bugg, J.D., Saad, G.A., 2002. The velocity field around a Taylor bubble rising in a stagnant viscous fluid: numerical and experimental results. *Int. J. Multiph. Flow* 25 (5), 791–803.
- Butler, C., Cid, E., Billet, A.-M., 2016. Modelling of mass transfer in Taylor flow: investigation with the PLIF-I technique. *Chem. Eng. Res. Des.* 115, 292–302.
- Charogiannis, A., An, J.S., Markides, C.N., 2015. A simultaneous planar laser-induced fluorescence, particle image velocimetry technique for the investigation of thin liquid-film flows. *Exp. Therm. Fluid Sci.* 68, 516–536.
- Dani, A., Guiraud, P., Cockx, A., 2007. Local measurement of oxygen transfer around a single bubble by planar laser-induced fluorescence. *Chem. Eng. Sci.* 62, 7245–7252.
- Fairbrother, F., Stubbs, A.E., 1935. Studies in electroendosmosis: the bubble method of measurement. *J. Chem. Soc.* 0, 527–529.
- Fletcher, D.F., Haynes, B.S., 2017. CFD simulation of Taylor flow: should the liquid film be captured or not? *Chem. Eng. Sci.* 167, 334–335.
- Gupta, R., Fletcher, D.F., Haynes, B.S., 2009. On the CFD modelling of Taylor flow in microchannels. *Chem. Eng. Sci.* 64, 2941–2950.
- Haase, S., Murzin, D.Y., Salmi, T., 2016. Review on hydrodynamics and mass transfer in minichannel wall reactors with gas–liquid Taylor flow. *Chem. Eng. Res. Des.* 113, 304–329.
- Häber, T., Gebretsadik, M., Bockhorn, H., Zarzalis, N., 2015. The effect of total reflection in PLIF imaging of annular thin films. *Int. J. Multiph. Flow* 76, 64–72.
- Haghnegahdar, M., Boden, S., Hampel, U., 2016. Investigation of mass transfer in milli-channels using high-resolution microfocus X-ray imaging. *Int. J. Heat Mass Transf.* 93, 653–664.
- Han, Y., Shikazono, N., 2009. Measurement of the liquid film thickness in a micro tube slug flow. *Int. J. Heat Fluid Flow* 30 (5), 842–853.
- Hassanvand, A., Hashemabadi, S.H., 2012. Direct numerical simulation of mass transfer from Taylor bubble flow through a circular capillary. *Int. J. Heat Mass Transf.* 55, 5959–5971.
- Hayashi, K., Hosoda, S., Schlüther, M., Tomiyama, A., 2014. Effects of shape oscillation on mass transfer from a Taylor bubble. *Int. J. Multiph. Flow* 58, 236–245.
- Heil, M., 2001. Finite Reynolds number effects in the Bretherton problem. *Phys. Fluids* 13 (9), 2517–2521.
- Hosoda, S., Abe, S., Hosokawa, S., Tomiyama, A., 2014. Mass transfer from a bubble in a vertical pipe. *Int. J. Heat Mass Transf.* 69, 215–222.
- Howard, J.A., Walsh, P.A., 2013. Review and extensions to film thickness and relative bubble drift velocity prediction methods in laminar Taylor or slug flows. *Int. J. Multiph. Flow* 55, 32–42.

- Huntsova, V., Gay, S., Nowak-Sliwinska, P., Rajendran, S.K., Zellweger, M., van den Bergh, H., Wagnières, G., 2014. In vivo measurements of tissue oxygenation by time-resolved luminescence spectroscopy: advantageous properties of dichlorotris(1,10-phenanthroline)-ruthenium(II) hydrate. *J. Biomed. Opt.* 19 (7), 077004.
- Janke, T., Bauer, K., 2017. Visualizing dissolved oxygen transport for liquid ventilation in an in vitro model of the human airways. *Meas. Sci. Technol.* 28, 055701.
- Jimenez, M., Dietrich, N., Grace, J.R., Hébrard, G., 2014. Oxygen mass transfer and hydrodynamic behaviour in wastewater: determination of local impact of surfactants by visualization techniques. *Water Res.* 58, 111–121.
- Jimenez, M., Dietrich, N., Hébrard, G., 2013. Mass transfer in the wake of non-spherical air bubbles quantified by quenching of fluorescence. *Chem. Eng. Sci.* 100, 160–171.
- Jimenez, M., Dietrich, N., Hébrard, G., Cockx, A., 2013b. Experimental study of O₂ diffusion coefficient measurement at a planar gas–liquid interface by planar laser-induced fluorescence with inhibition. *AIChE J.* 59, 325–333.
- Johnson, T.A., Pattel, V.C., 1999. Flow past a sphere up to a Reynolds number of 300. *J. Fluid Mech.* 378, 19–70.
- Kastens, S., Hosoda, S., Schlüter, M., Tomiyama, A., 2015. Mass transfer from single Taylor bubbles in minichannels. *Chem. Eng. Technol.* 38 (11), 1925–1932.
- Kastens, S., Meyer, C., Hoffmann, M., Schlüter, M., 2017. Experimental investigation and modelling of local mass transfer rates in pure and contaminated Taylor flows. In: Bothe, D., Reusken, A. (Eds.), *Transport Processes at Fluidic Interfaces. Advances in Mathematical Fluid Mechanics*. Cham, Birkhäuser, pp. 609–637.
- King, C., Walsh, E., Grimes, R., 2007. PIV Measurements of flow with plugs in a microchannel. *Microfluid. Nanofluid.* 3, 463–472.
- Kreutzer, M.T., Kapteijn, F., Moulijn, J.A., Heiszwolf, J.J., 2005. Multiphase monolith reactors: chemical reaction engineering of segmented flow in microchannels. *Chem. Eng. Sci.* 60, 5895–5916.
- Kurimoto, R., Nakazawa, K., Minagawa, H., Yasuda, T., 2017. Prediction models of void fraction and pressure drop for gas–liquid slug flow in microchannels. *Exp. Therm. Fluid Sci.* 88, 124–131.
- Liu, H., Vandu, C.O., Krishna, R., 2005. Hydrodynamics of Taylor flow in vertical capillaries: flow regimes, bubble rise velocity, liquid slug length, and pressure drop. *Ind. Eng. Chem. Res.* 44, 4884–4897.
- Mac Giolla Eain, M., Egan, V., Punch, J., 2013. Film thickness measurements in liquid–liquid slug flow regimes. *Int. J. Heat Fluid Flow* 44, 515–523.
- Machado, R.M., Broekhuis, R.R., Nordquist, A.F., Roy, B.P., Carney, S.R., 2005. Applying monolith reactors for hydrogenations in the production of specialty chemicals – process and economic considerations. *Catal. Today* 105, 305–317.
- Meyer, C., Hoffman, M., Schlüter, M., 2014. Micro-PIV analysis of gas–liquid Taylor flow in a vertical orientated square shaped fluidic channel. *Int. J. Multiph. Flow* 67, 140–148.
- Nakamaru, K., 1982. Synthesis, luminescence quantum yields, and lifetimes of trischelated ruthenium(II) mixed-ligand complexes including 3,3'-dimethyl-2,2'-bipyridyl. *Bull. Chem. Soc. Jpn.* 55, 2697–2705.
- Nogueira, S., Riethmuller, M.L., Campos, J.B.L.M., Pinto, A.M.F.R., 2006. Flow patterns in the wake of a Taylor bubble rising through vertical columns of stagnant flowing newtonian liquids: an experimental study. *Chem Eng Sci* 61, 7199–7212.
- O'Neal, P., Meledeo, A., Davis, J.R., Ibey, B.L., Gant, V.A., Pishko, M.V., Coté, G.L., 2004. Oxygen sensor based on the fluorescence quenching of a ruthenium complex immobilized in a biocompatible poly (ethylene glycol) hydrogel. *IEEE Sens J* 4 (6), 728–734.
- Roudet, M., Billet, A.-M., Cazin, S., Risso, F., Roig, V., 2017. Experimental investigation of interfacial mass transfer mechanisms for a confined high-reynolds-number bubble rising in a thin gap. *AIChE J.* 63 (6), 1547–5905.
- Sander, R., 2015. Compilation of Henry's law constants (version 4.0) for water as solvent. *Atmos. Chem. Phys.* 15, 4399–4981.
- Sciacchitano, A., Wieneke, B., 2016. PIV Uncertainty propagation. *Meas. Sci. Technol.* 27 (8), 084006.
- Settles, G.S., 2001. *Schlieren and Shadowgraphy Techniques: Visualizing Phenomena in Transport Media*. Springer-Verlag Berlin Heidelberg GmbH, New York.
- Shao, N., Gavriilidis, A., Angeli, P., 2010. Mass transfer during Taylor flow in microchannels with and without chemical reaction. *Chem. Eng. J.* 160, 873–881.
- Sobieszuk, P., Aubin, J., Pohorecki, R., 2012. Hydrodynamics and mass transfer in gas–liquid flows in microreactors. *Chem. Eng. Technol.* 35 (8), 1346–1358.
- Taylor, G.I., 1961. Deposition of a viscous fluid on the wall of a tube. *J. Fluid Mech.* 10 (2), 161–165.
- Thulasidas, T.C., Abraham, M.A., Cerro, R.L., 1997. Flow patterns in liquid slugs during bubble–train flow inside capillaries. *Chem. Eng. Sci.* 52 (17), 2947–2962.
- Tsoligkas, A.N., Simmons, M.J.H., Wood, J., 2007. Influence of orientation upon the hydrodynamics of gas–liquid flow for square channels in monolith supports. *Chem. Eng. Sci.* 62, 4365–4378.
- Valiorgue, P., Souzy, N., El Hajem, M., Ben Hadid, H., Simoëns, S., 2013. Concentration measurement in the wake of a free rising bubble using planar laser-induced fluorescence (PLIF) with a calibration taking into account fluorescence extinction variations. *Exp. Fluids* 54, 1–10.
- Van Baten, J.M., Krishna, R., 2004. CFD simulations of mass transfer from Taylor bubbles rising in circular capillaries. *Chem. Eng. Sci.* 59 (12), 2535–2545.
- Van Hout, R., Gulitski, A., Barnea, D., Shemer, L., 2002. Experimental investigation of the velocity field induced by a Taylor bubble rising in stagnant water. *Int. J. Multiph. Flow* 25 (4), 579–596.
- Vandu, C.O., Liu, H., Krishna, R., 2005. Mass transfer from Taylor bubbles rising in circular capillaries. *Chem. Eng. Sci.* 60, 6430–6437.
- Webster, D.R., Roberts, P.J.W., Ra'ad, L., 2001. Simultaneous DPTV/PLIF measurements of a turbulent jet. *Exp. Fluids* 30, 65–72.
- Xu, F., Jimenez, M., Dietrich, N., Hébrard, G., 2017. Fast determination of gas–liquid diffusion coefficient by an innovative double approach. *Chem. Eng. Sci.* 170, 68–76.
- Yang, L., Dietrich, N., Loubière, K., Gourdon, C., Hébrard, G., 2016. Visualization and characterization of gas–liquid mass transfer around a Taylor bubble right after the formation stage in microreactors. *Chem. Eng. Sci.* 143, 364–368.